Scale Invariance of Liquid Water Distributions in Marine Stratocumulus. Part I: Spectral Properties and Stationarity Issues

ANTHONY DAVIS,* ALEXANDER MARSHAK,* WARREN WISCOMBE, AND ROBERT CAHALAN

Climate and Radiation Branch, NASA/Goddard Space Flight Center, Greenbelt, Maryland

(Manuscript received 12 June 1995, in final form 5 December 1995)

ABSTRACT

This study investigates the internal structure of marine stratocumulus (Sc) using the spatial fluctuations of liquid water content (LWC) measured along horizontal flights off the coast of southern California during the First ISCCP Regional Experiment (FIRE) in summer of 1987. The results of FIRE 87 data analyses are compared to similar ones for marine Sc probed during the Atlantic Stratocumulus Transition Experiment (ASTEX) in summer 1992 near the Azores. In this first of two parts, the authors use spectral analysis to determine the main scale-invariant regimes, defined by the ranges of scales where wavenumber spectra follow power laws; from there, they discuss stationarity issues. Although crucial for obtaining meaningful spatial statistics (e.g., in climate diagnostics), the importance of establishing stationarity—statistical invariance under translation—is often overlooked. The sequel uses multifractal analysis techniques and addresses intermittency issues. By improving our understanding of both nonstationarity and intermittency in atmospheric data, we are in a better position to formulate successful sampling strategies.

Comparing the spectral responses of different instruments to natural LWC variability, the authors find scale breaks (characteristic scales separating two distinct power law regimes) that are spurious, being traceable to well-documented idiosyncrasies of the Johnson–Williams probe and forward scattering spectrometer probes. In data from the King probe, the authors find no such artifacts; all spectra are of the scale-invariant form $k^{-\beta}$ with exponents β in the range 1.1–1.7, depending on the flight. Using the whole FIRE 87 King LWC database, the authors find power-law behavior with $\beta = 1.36 \pm 0.06$ from 20 m to 20 km. From a spectral vantage point, the ASTEX cloud system behaves statistically like a scaled-up version of FIRE 87: a similar exponent $\beta = 1.43 \pm 0.08$ is obtained, but the scaling range is shifted to [60 m, 60 km], possibly due to the 2–3 times greater boundary layer thickness.

Finally, the authors reassess the usefulness of spectral analysis:

- Its main shortcoming is ambiguity: very different looking stochastic processes can yield similar, even identical, spectra. This problem impedes accurate modeling of the LWC data and, ultimately, is why multifractal methods are required.
- Its main asset is applicability in stationary and nonstationary situations alike and, in conjunction with scaling, it can be used to detect nonstationary behavior in data.

Having $\beta > 1$, LWC fields in marine Sc are nonstationary within the scaling range and stationary only at larger scales. Nonstationarity implies long-range correlations, and we demonstrate the damage these cause when trying to estimate means and standard deviations with limited amounts of LWC data.

1. Introduction and overview

Clouds have a first-order effect on the earth's radiative budget (Ramanathan et al. 1989) and are the major source of uncertainty in climate modeling (Cess et al. 1989). Current climate models assume clouds are plane-parallel, horizontally homogeneous sheets; at best, a linear combination of cloudy and clear portions according to cloud fraction is used to account for horizontal inhomogeneity when predicting radiative properties. This motivates us to better understand cloud structure. Marine stratocumulus (Sc) are a good starting point. They are one of the most studied cloud types, partly because they exert a systematic effect on the global radiation budget. Phase I of the First ISCCP (International Satellite Cloud Climatology Project) Research Experiment (FIRE) field program (Albrecht et al. 1988), which took place over the Pacific Ocean off San Diego in summer 1987, was entirely devoted to these unusually persistent and horizontally extended clouds. Phase II of FIRE, operating in tandem with the Atlantic Stratocumulus Transition Experiment (ASTEX) in summer 1992 over the Atlantic Ocean near

* Additional affiliation: Science Systems and Applications, Inc., Lanham, Maryland.

Corresponding author address: Dr. Anthony Davis, NASA/GSFC, Code 913, Greenbelt, MD 20771.
E-mail: davis@climate.gsfc.nasa.gov

the Azores, continued and extended the FIRE 87 studies by focusing on the Sc to cumulus transition.

Cahalan and Snider (1989) obtained probability distributions and wavenumber spectra for vertically integrated liquid water path (LWP) measured by microwave radiometry during FIRE 87. Cahalan et al. (1994a) developed a fractal cascade model for the optical depth field based on these LWP statistics. By way of Monte Carlo simulations (Cahalan et al. 1994b), this model enabled them to show that standard plane-parallel radiative transfer theory based only on the mean optical depth leads to serious errors in Sc cloud albedo. Cahalan et al. thus established that statistics beyond the mean are necessary to get Sc radiation effects right in models; they conclude that we also need to know, at the very least, the variance of log(LWP) and the spectral exponent (absolute slope β of the wavenumber spectrum in log–log axes, discussed extensively further on).

We expand upon the data analysis begun by Cahalan and Snider in a variety of ways. First, we will consider aircraft LWC data rather than ground-based LWP data, which are not typically sampled at the high spatial frequencies achieved on aircraft. Our main goal is an improved statistical characterization of internal marine Sc structure (in terms of LWC distribution), a prerequisite for developing better cloud models and, in turn, furthering our understanding of cloud radiation properties. To this effect, we apply a battery of data analysis techniques to liquid water time series from FIRE 87 and ASTEX that go far beyond probability distribution functions (pdf's) and wavenumber spectra, in the following ways:

- Following a well-established tradition in turbulence research, we systematically compile statistical information on a scale by scale basis. In this first part, we use primarily spectral analysis, a conventional way of doing scale by scale analysis in Fourier space, where the scale parameter is either the wavenumber k or $r = 1/k$.
- We seek simple connections that relate properties at one scale to another. The current paradigm is to seek "scaling" behavior, that is, power laws in the scale parameter. The important quantity is then the *exponent* of the power law. We take special care in how exponent values are determined numerically and how uncertainties are assigned to them.
- We assess the practical importance of the statistics we introduce. In this first part we assess the information conveyed by spectral analysis and find that, unlike some techniques implemented in physical space, spectral analysis is applicable to both stationary and nonstationary regimes. When scaling prevails, this allows us to empirically differentiate between the two regimes, measure the degree of nonstationarity, and detect transitions from one regime to the other. This is important because stationary and nonstationary regimes call for rather different statistical treatments. Several theoretical and LWC-based examples of stationary and nonstationary behaviors are discussed.
- We will assess a statistic's sensitivity to the occurrence of a single strong feature in the data. Such a rare event could be a harbinger of true intermittency or merely a glitch in the datastream (a short sequence of corrupted values); it is therefore desirable to have both insensitive statistical quantities and sensitive ones, to draw our attention to potential spurious values in the data.

In the next section, we survey some important scaling concepts and how they have permeated cloud morphology studies in the past decade or so. In section 3, we define our notations and terminology for scale-invariant spectral analysis. The spectral responses of King, forward scattering spectrometer probe (FSSP), and Johnson–Williams (J–W) probes to LWC variability during FIRE 87 are compared in section 4, where a rationale is presented for retaining only King data in the remainder of the paper. In section 5, we describe and visualize the five King LWC datasets, discuss sampling issues, and compare their individual spectra, using guidelines for statistical noise reduction and exponent determination detailed in appendix A. Ensemble-average spectra for FIRE 87 and ASTEX are compared in section 6, revealing interesting similarities and differences that are interpreted in dynamical terms. Drawing on tutorial material from appendix B, section 7 discusses some important implications in physical space of scaling in Fourier space in terms of "statistical stationarity" and "stochastic continuity," both concepts are illustrated with LWC data. Finally, we summarize our findings in section 8.

In Part 2 (Marshak et al. 1995, submitted to *J. Atmos. Sci.*), we pursue our investigation of the scale-invariant properties of LWC in marine Sc using the King data by applying "multifractal" methods that are implemented in physical (rather than Fourier) space. This enables us to address intermittency issues and thus to escape the Gaussian paradigm that underlies most standard statistics, including spectral analysis by itself. We will show that nonstationarity and intermittency are complementary features of the atmospheric data. The multifractal techniques used in Part 2 are also effective in helping to find the strong events, which are possibly instrumental glitches.

2. Background

There is a growing awareness of the need to study atmospheric phenomena at several widely separated scales at once (e.g., Sui and Lau 1992; Weng and Lau 1994). Geophysical systems in general naturally spawn structures over a wide range of scales, so the first step in our search for a physically sound approach to LWC data analysis is to use statistics based on scale, a key parameter that we will denote r. We call this scale by

scale statistical analysis. Our next step is to seek power-law behavior (or "scaling") with respect to r. In this, we are following a method whereby turbulent flows were successfully investigated over the last few decades.

The physical meaning we can attribute to a statistical power law in r is that the same physical processes dominate over the associated range of scales $[\eta, R]$. Smaller parts of the system therefore look like scaled-down larger parts, and vice versa. The connection to fractal geometry, where the same geometric operation is recursively performed at finer and finer scales, is straightforward. Realistic cloud scenes can be artificially generated merely by adding an element of randomness to algorithms for generating deterministic fractals (e.g., Lovejoy and Mandelbrot 1985; Peitgen and Saupe 1988), which further motivates us to use a combination of scaling methodology and statistics.

A power-law statistic $\propto r^{\alpha}$ is invariant under a change of scale $r \to \lambda r$ in the sense that only the scale ratio λ and the exponent α are required to predict the new value. This contrasts strongly with a statistic where one (or more) special scale(s) occur, for example, $\propto \exp(-r/r^*)$, because its value at two arbitrary scales can only be compared by first comparing the two scales to the special one(s). Observation of a power law in r therefore reflects a statistical invariance or symmetry under change of scale, called scale invariance or just scaling. If robust (persistent under addition of more data), breaks in the scaling symmetry are important since they indicate a change in the dominant physical process in the system.

Lovejoy (1982) was the first to study the random fractal structure of clouds and rain. Since then, such studies in morphology have become quite popular (e.g., Rys and Waldvogel 1986; Yano and Takeuchi 1987; Cahalan and Joseph 1989; Sèze and Smith 1990). In addition, clouds were probed internally by aircraft, revealing variability over all observable scales. To the best of our knowledge, the first quantitative evidence of scaling in a cloud LWC field was reported by King et al. (1981), who argued the quality of their hot-wire probe using the excellent scaling in the LWC wavenumber spectrum. Since then, optical Knollenberg probes or FSSPs have enjoyed an increasing popularity among cloud physicists because of their ability to measure the complete droplet size distribution. Using FSSP data, Duroure and Guillemet (1990) found scaling in the spatial distribution of clear to cloudy air interfaces, as defined by a threshold in the total droplet count. Their results were extended by Malinowski and Zawadzki (1993), who applied box-counting as well as histogram techniques to LWC and to total droplet count. Baker (1992) found considerable centimeter-scale inhomogeneity in the Poissonian characteristics of FSSP droplet arrival times. Malinowski et al. (1992) and Malinowski and Zawadzki (1993) applied fractal analyses to the same type of data and confirmed the high level of small-scale variability.

3. Scale invariance in Fourier space

Let $\tilde{\varphi}(k)$, $-\infty < k < \infty$, be the Fourier transform of a stochastic process $\varphi(x)$, $0 \leq x \leq L$. The energy spectrum $E(k)$ of $\varphi(\cdot)$ is defined as

$$E(k) = \frac{1}{L}\langle|\tilde{\varphi}(k)|^2 + |\tilde{\varphi}(-k)|^2\rangle, \quad k > 0, \quad (1)$$

where $\langle\cdot\rangle$ designates ensemble averaging, that is, averaging over all possible realizations of $\varphi(\cdot)$. We will use the expressions wavenumber spectrum or energy spectrum interchangeably to designate $E(k)$, noting that it is also referred to as the power spectrum, variance spectrum, periodogram, and spectral density.

A common application of spectral analysis is to locate dominant frequencies, wherever $E(k)$ has a peak rising unambiguously above the background. Scales $r = 1/k$ can be special in other ways, for example, the upper and lower scales bounding a scale-invariant regime; between these bounds the energy spectrum follows a power law:

$$E(k) \propto k^{-\beta}. \quad (2)$$

For theoretical models, one can obtain $E(k)$ in (1), hence β in (2), either analytically or numerically. For data, we generally have only a small number of realizations or experiments with a finite spatial sampling, assumed uniform: $\varphi_i = \varphi(x_i)$, $x_i = il$ $(i = 1, \cdots, N_{\text{tot}})$, where l is the sampling scale and N_{tot} is the number of points. Of these, $N_2 = 2^{[\log N_{\text{tot}}]}$, $[\cdot]$ meaning integer part, are used at a time in fast Fourier transform (FFT) computations, for an overall length $L_2 = N_2 l$.

We now put spectral analysis and the power-law parameterization of $E(k)$ in Eq. (2) to work in three comparative studies: first, of the three LWC instruments used during FIRE 87 (section 4); then, of the five flights where the King probe was operational (section 5); finally, of the ensemble-average spectra for FIRE 87 and ASTEX (section 6).

4. Spectral responses of different LWC probes to natural variability

In all, we investigated 13 LWC datasets, all from the FIRE 87 database, furnished to us from the National Center Atmospheric Research (NCAR) through P. Austin: 3 from the J–W hot-wire probe, all collected on 30 June by the C-130 aircraft and 5 each from the Knollenberg FSSP and the King hot-wire probe. Figure 1 shows typical LWC output from J–W and FSSP devices and King data. The FSSP and simultaneous King data in Figs. 1b and 1c were both collected on the 2 July Electra flight. Figure 2 compares the energy spectra in log–log axes for the datasets displayed partially in Fig. 1.

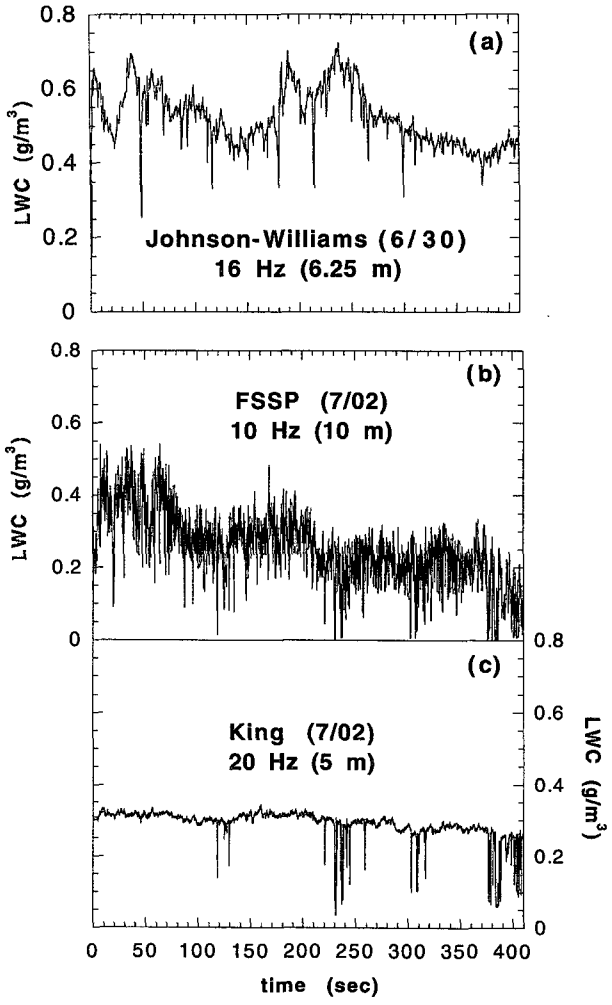

FIG. 1. Typical LWC time series from the J–W, Knollenberg (FSSP), and King probes. (a) A time series 410 s long from the J–W hot-wire probe, sampled at 16 Hz on board the C-130 aircraft on 30 June 1987, starting at 2053 UTC. (b) Another time series of equal length but sampled at 10 Hz, from the FSSP on board the NCAR Electra on 2 July, starting at 0223 UTC; (c) time-registered data from the collocated King probe, sampling at 20 Hz. Overall, these two last instruments deliver comparable values, but noise contamination is obvious in the small-scale variability of the FSSP data. Spatial sampling scales are indicated, assuming a nominal aircraft speed of 100 m s^{-1}.

Compared to the King data, the FSSP data in Fig. 1b has a large noise component that overwhelms the delicate small-scale features, particularly, the downward spikes. Accordingly, the King and FSSP spectra have similar slopes only for scales larger than ~250 m; below that the FSSP spectrum flattens out toward a (stationary) white noise spectrum. To illustrate this, we added Gaussian white noise at the 5% level to the King 2 July dataset and plotted its energy spectrum in Fig. 2.

The FSSP's elementary sampling volume is so small that an accurate droplet distribution, from which LWC is calculated as its third moment, can be captured only every few hundred meters. Baker (1992) uses FSSP data nevertheless to detect smaller-scale variability by (i) focusing on the droplet number concentration (counting drops is a lot more reliable than sizing them in an FSSP) and (ii) relying on sophisticated statistical analyses of the raw signal (arrival and departure times of individual droplets in the instrument's laser beam). Furthermore, Brenguier (1992) describes a "fast" FSSP that uses real-time software control to overcome some of the instrument's limitations; using this technique, Rodi et al. (1992) obtain power-law energy spectra down to the smallest scales.

The J–W instrument suffers from a different problem at small scales. Its hot wire has more thermal inertia than the King probe's, hence a tendency toward more smoothness—and a steeper spectrum—for scales smaller than ~500 m. Above 500 m, the J–W spectral exponents roughly match those of the FSSP and King probe. In Fig. 1a we still see the downward spikes; they "hang" however from higher baseline values than in Fig. 1a for the King data. Such large offsets are not seen between the King and FSSP data.

Summarizing, the King probe is the most reliable and diverse source of information on small-scale variability in marine Sc in the FIRE 87 database, so it is used exclusively in the remainder of this paper and its se-

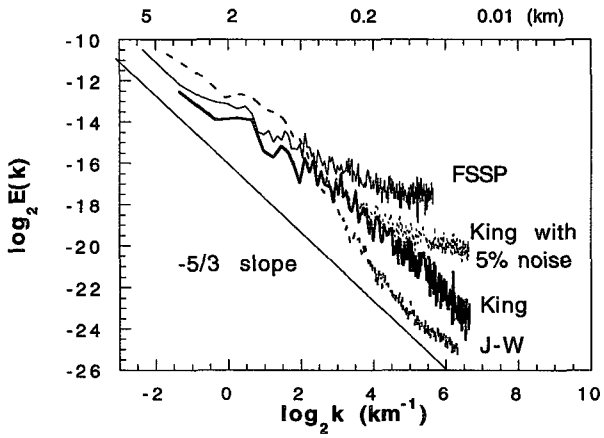

FIG. 2. Spectra of J–W, FSSP, and King LWC data. All spectra consist of 256 wavenumbers but cover somewhat different ranges of scales due to the different sampling rates: from 10 m to 2.6 km for the King probe, from 20 m to 5.1 km for the FSSP, and from 12.5 m to 3.2 km for the J–W probe. The three instruments more or less agree for the largest scales: $k < 4$ km^{-1}, therefore $r = 1/k > 250$ m. On the one hand, the J–W hot-wire probe is then effectively operating at a lower frequency, unaffected by the characteristic smoothing due to the greater thermal inertia than its King counterpart. On the other hand, the FSSP is then counting enough droplets throughout the size distribution to make reasonable estimates of its third moment, the local large-scale mean LWC. For small scales, the FSSP data is clearly contaminated by white (uncorrelated) noise of instrumental origin; an FSSP-type spectrum is simulated by adding white noise to the King data, but the ±5% level used in the figure is far too conservative.

quel. The new PVM-100 liquid water probe has cleaner optically based physics than hot-wire probes and a sampling volume 10^4 times larger than a typical FSSP (Gerber et al. 1994) but it was not available until the ASTEX experiment in 1992.

5. Statistical variability of King LWC data from FIRE 87

a. Description and visualization

The LWC measurements we use in the remainder of this section were obtained during FIRE 87 from a King probe on the NCAR Electra aircraft. King et al. (1978, 1981) describe the basic design, electronic control, and calibration of this LWC probe. The power required to maintain the temperature of a wire on which droplets are impacting is recorded and eventually converted into LWC in g m^{-3}. The device has a sensitivity of 0.02 g m^{-3}, a response time of ~0.05 s, and an accuracy of ~5% at 1 g m^{-3}.

We investigate five different King probe time series, the longest in-cloud datasets, giving us access to the largest range of scales. Their more important characteristics are listed in Table 1; for further information, such as flight tracks, we refer to Kloesel et al. (1988). Some flight tracks were not straight throughout the probing, but no leg was less than an integral (correlation) length scale, so the time series can be viewed as 1D transects of the LWC under Taylor's frozen turbulence hypothesis. The horizontal flight legs used here were at roughly midcloud or slightly above, as determined from Austin et al.'s (1995) estimates of cloudbase height and cloud thickness for the first, third, and fifth cases. Figures 3a–e display representative fragments consisting of $2^{13} = 8192$ points. The accompanying one-point pdf's show a pronounced negative skewness due to the downward spikes in three of the five cases (a, b, and d). These downspikes are probably dry air entrained from cloud top and carried by penetrating downdrafts.

Figure 3c (14 July) has two striking features: first, a degree of homogeneity that prevails over the remainder of this long dataset; second, a sudden dip from over 0.3 g m^{-3} to less than 0.1 g m^{-3}. This dataset accounts for ~50% of all the King probe record; however, its 330-km length is still dwarfed by the size of marine Sc systems, which can extend for thousands of kilometers. We suspect that the dip is an instrumental glitch but are unable to rule out a physical cause since negative fluctuations just as deep, almost as wide, but not quite as abrupt, occur in the other datasets. To illustrate this point, Fig. 4a shows a zoom onto the alleged glitch and on another narrower and less intense dip from the same dataset (not illustrated in Fig. 3c), while Fig. 4b shows down spikes of roughly the same width extracted from Fig. 3a. If the dips in Figs. 3c and 4a are spurious, we must ask ourselves what would have happened if it failed to be screened out. We will therefore closely follow the effect of this dip in the statistics described below.

Figure 3d is like a juxtaposition of the types of data in Figs. 3a and 3b with that in Fig. 3c, with exaggerated variability in the left half and almost no variability in the right half. Finally, the data in Fig. 3e is also intriguing, its one-point pdf being bimodal and positively skewed.

b. Sampling issues

"Stationarity" is not an attribute one would use intuitively to describe Figs. 3d and 3e. Technically, stationarity means invariance of statistical properties under translation. In practice, this means that we should be able to obtain reasonably accurate estimates of (climatological) averages using reasonable amounts of data. To illustrate this point quantitatively, we define the running mean over scale r, starting at position x, of some function $\varphi(x)$ defined for $0 \leq x \leq L$:

$$m_\varphi(r, x) = \frac{1}{r}\int_x^{x+r} \varphi(x')dx', \tag{3a}$$

for $0 < r \leq L$, $0 \leq x \leq L - r$; and similarly the running variance

$$\sigma_\varphi(r, x)^2 = \frac{1}{r}\int_x^{x+r} [\varphi(x') - m_\varphi(r, x)]^2 dx' = \frac{1}{r}\int_x^{x+r} \varphi(x')^2 dx' - m_\varphi(r, x)^2. \tag{3b}$$

TABLE 1. Characteristics of the FIRE 87 King LWC datasets. The total of 130 804 data points were collected during the FIRE 1987 stratocumulus experiment, off San Diego, California. An aircraft speed of 100 m s^{-1} was used to convert time to space, the sampling rate being 20 Hz (hence a distance $l = 5$ m). The integer part $[\log_2 N_{tot}]$ of the fourth column yields $N_2 = 2^{[\log_2 N_{tot}]}$, the maximum number of points used in the FFTs; the corresponding length is denoted $L_2 = N_2 l$.

Date (1987)	Time (UTC)	N_{tot} (points)	$\log_2 N_{tot}$	Length L (km)	Altitude (m)	Character	Comment
30 June	2241	28 672	14.81	143	790	spiky	downward
2 July	0223	16 384	14	82	770	spiky	downward
14 July	1818	65 536	16	328	700	smooth	suspicious dips
16 July	1717	8192	13	41	625	mixed	spikes down
16 July	1819	12 020	13.55	60	630	mixed	spikes up

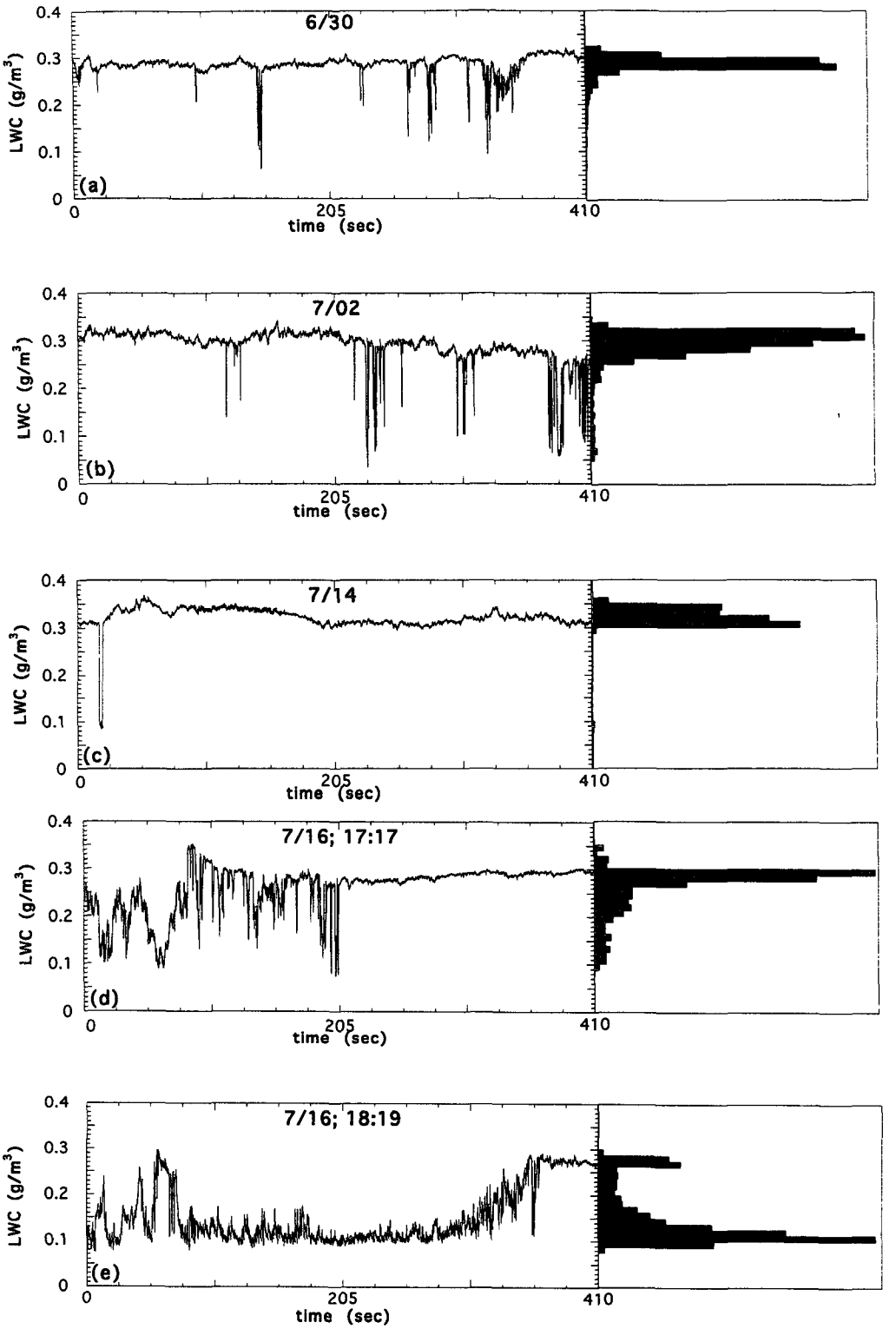

FIG. 3. Representative portions of five King LWC datasets from FIRE, June–July 1987. (a) 30 June, (b) 2 July, (c) 14 July, (d) 1717 UTC 16 July, and (e) 1819 UTC 16 July. The data was collected at constant altitude with the King probe carried by the NCAR Electra. All portions are roughly 41 km long (exactly 2^{13} = 8192 points sampled at 20 Hz). The histograms show the corresponding LWC field's one-point probability density function, dividing the overall range 0.0–0.4 g m^{-3} into 22 bins.

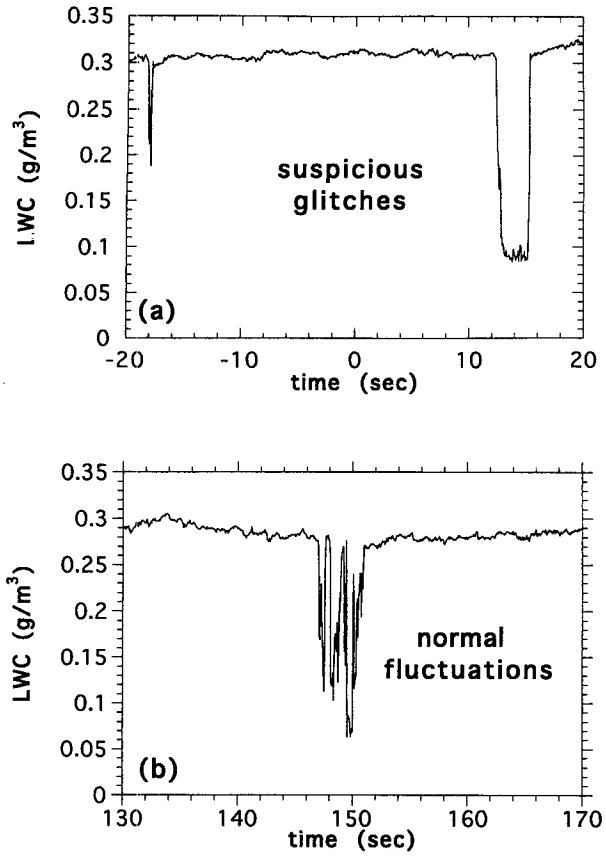

FIG. 4. Blowup of two alleged glitches and normal downspikes. (a) Two suspicious events in the 14 July data, partially displayed in Fig. 3c. (The leftmost glitch is outside Fig. 3c, hence the negative time of occurrence.) (b) A cluster of normal downspikes from Fig. 3a.

Figure 5a shows $m_\varphi(r, 0)$ for the five LWC datasets in Table 1. Only three seem to converge—stop varying as r increases—at all (the data in Figs. 3d and 3e do not). Only two of these end up close to the overall mean $\langle \mathrm{LWC} \rangle \approx 0.29$ g cm^{-3}, our estimate of the climatology. Only one of these (30 June) remains close to $\langle \mathrm{LWC} \rangle$ for all scales. Another dataset (1819 UTC 16 July) ends at almost two (ensemble based) σ_{LWC}'s below $\langle \mathrm{LWC} \rangle$. Even the longest dataset (14 July) ends about $\sigma_{\mathrm{LWC}}/2$ above $\langle \mathrm{LWC} \rangle$. Such lack of convergence and/or sample to sample variability is typical of nonstationary processes. We would never be able to estimate $\langle \mathrm{LWC} \rangle$ without all of our five datasets, nor the sample mean $m_\varphi(L, 0)$ with a dataset of length $L < 50$ km or so. Even with five datasets, we cannot guarantee 0.29 g cm^{-3} as the climatological mean, robust with respect to the addition of more data from the same type of cloud.

Running standard deviations $\sigma_\varphi(r, 0)$, the other member of the Gaussian pair of statistical parameters, for the same five LWC datasets are plotted in Fig. 5b. We see that only the long/smooth 14 July dataset has apparently converged, however to a value that underestimates σ_{LWC} (obtained from all the datasets combined) by a factor of 3. The 1717 and 1819 UTC 16 July datasets give the best single-run estimates for this second order statistic, precisely the datasets that produce the worst estimates of $\langle \mathrm{LWC} \rangle$. A striking feature of the $\sigma_\varphi(r, 0)$ graphs is the way new levels of variance are reached by substantial jumps. Clearly, these quasi

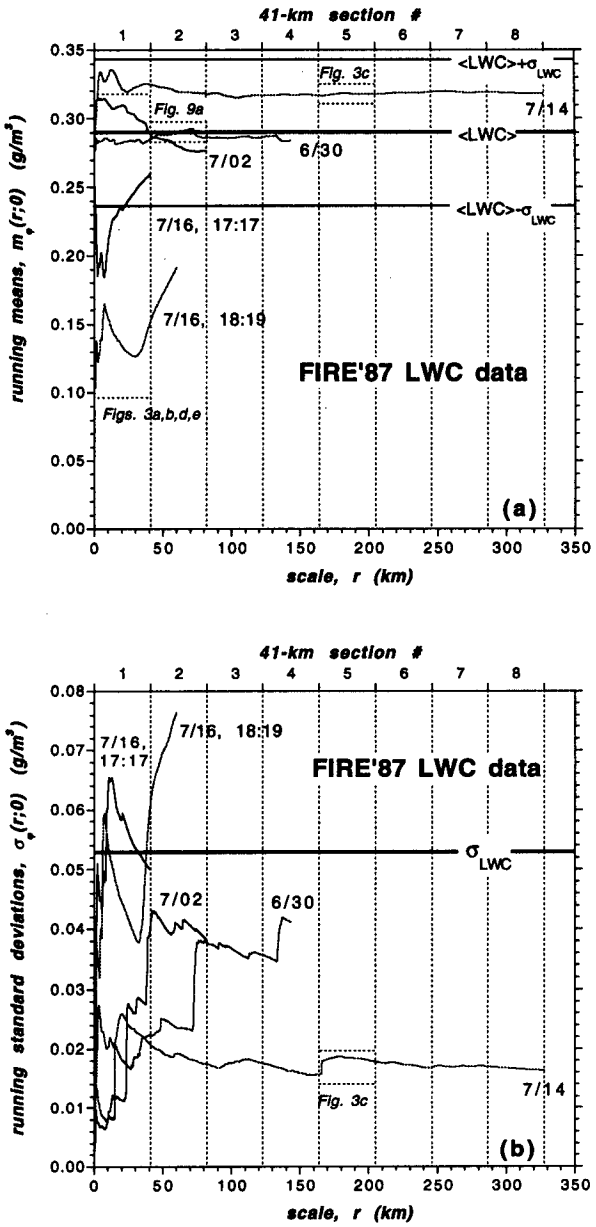

FIG. 5. Gaussian statistics of LWC as a function of scale r and realization. (a) Running means starting at the origin, $m_{\mathrm{LWC}}(r, 0)$; the ensemble mean $\langle \mathrm{LWC} \rangle$ and $\langle \mathrm{LWC} \rangle \pm \sigma_{\mathrm{LWC}}$ (ensemble standard deviation) are indicated at the right. The portions illustrated in Figs. 3a–e and 9a are highlighted. (b) As in (a) but for running standard deviations $\sigma_{\mathrm{LWC}}(r, 0)$.

discontinuities are caused by the spikes in data, whereas the intervening, ever-slower decays and plateaus correspond to the smooth periods. Such strong localized events are uncharacteristic of processes obeying Gaussian statistics.

If the spatial statistics of a random function $\varphi(x)$, $0 \leq x \leq L$, converge to their ensemble average values as L becomes large, then $\varphi(x)$ is called ergodic. For all practical purposes, this is not the case for any of our LWC datasets, either because their running means and standard deviations have not converged at all or, if they have, to a different value from one dataset to the next. From our discussion of $m_\varphi(r, x)$ and $\sigma_\varphi(r, x)$, we can see that two kinds of sampling issues must be addressed:

- Can we say that a given dataset is long enough to yield meaningful (i.e., stable) spatial statistics of a given kind (e.g., Gaussian)?
- Do we have enough data, all datasets combined, to sample all the events that we are potentially interested in?

Ideally, we should ask ourselves these questions before collecting the data, in the planning stages of a field experiment. The former question is an issue of stationarity and it will be addressed in this paper from the standpoint of Gaussian statistics such as $m_\varphi(r, x)$ and $\sigma_\varphi(r, x)$; we return to these, as functions of x, after examining the spectral properties of LWC fields. The latter and more open-ended question raises the issue of ergodicity violation (sample to sample variability) due largely to the intermittent occurrence of intense events (large jumps, strong spikes, etc.).

c. *Individual spectra in two different representations*

The interested reader is referred to appendix A for a detailed description of two methods of reducing statistical noise in energy spectra that can be used in combination with a variety of ways of determining the spectral exponent β, also described in more or less detail. The intrinsic spectral properties of the different datasets are best compared by keeping to the same method of estimating $E(k)$ and β; we start in Fig. 6a with noise reduction method 1 (subdivision) and, for simplicity, an unweighted least squares regression to a linear function in the logs. The five spectra in Fig. 6a use $N_p = 512$ data points (256 wavenumbers), which corresponds to the distance between two minor ticks in Figs. 3a–e ($\approx$2.6 km). They show little noise, being averaged over $N_s = 32$ (30 June, 2 July), $N_s = 128$ (14 July), or $N_s = 16$ (16 July) subsets; the spectral exponent β ranges from 1.45 (1819 UTC 16 July, Fig. 3e) to 1.72 (1717 UTC 16 July, Fig. 3d).

In contrast, the spectra in Fig. 6b are obtained by noise reduction method 2 (octave binning) and show a similar but somewhat lower range of β, from 1.19 (2 July, Fig. 3b) to 1.68 (14 July, Fig. 1c), using the same type of regression. Notice the different wavenumber ranges for the different datasets. An important feature of this method is that the extreme slopes are closer to what we expect from a subjective classification: spikiness (concentrated energy at small scales) yields a

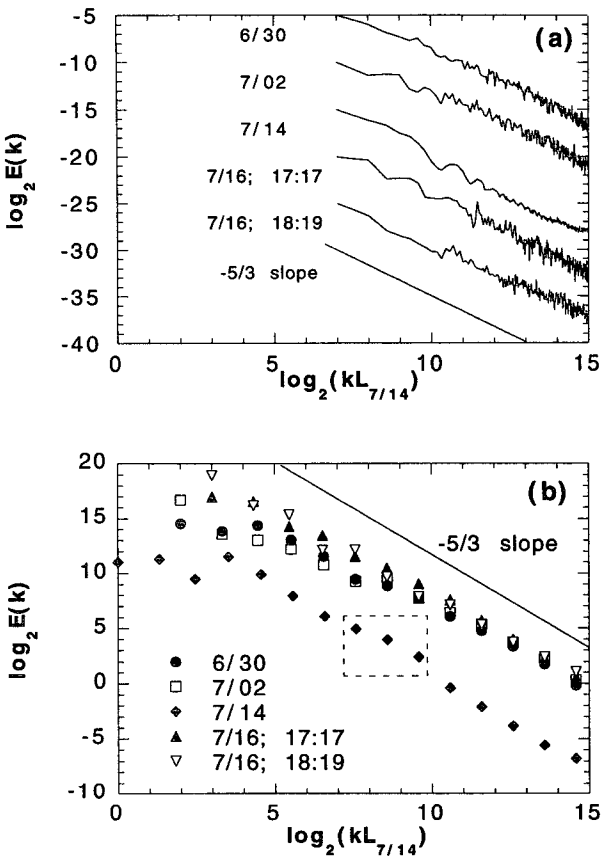

FIG. 6. (a) Energy spectra for FIRE 87 LWC in marine Sc, using standard noise reduction. All five datasets are treated according to the subdivision method with $N_p = 512$ points held constant, that is, averaging over enough subsets to end up with better defined $E(k)$'s for exactly 256 wavenumbers covering a range of scales from the inverse Nyquist frequency $2l = 10$ m to 2.56 km, two minor ticks in Figs. 3a–e. This is done by varying the input parameter $N_s = [N_{tot}/N_p]$ in the subroutine SPCTRM according to Table 2. (b) Energy spectra for FIRE 87 LWC in marine Sc, using octave binning. As in Fig. 6a except that the method of octave bins is used, yielding only $[\log_2 N_{tot}] - 1$ estimates of $E(k)$ but more broadly spaced, almost equally on the log scale. Notice the different minima in wavenumber value $1/L_2$, where $L_2 = N_2 l$ (cf. Table 1). At large scales ($k \leq 2^4/L_{2,7/14}$), three of the five datasets (bold symbols) show a leveling off in $E(k)$, giving us an estimate $R \approx L_{2,7/14}/2^4 \approx 20$ km for the integral scale of LWC fluctuations in marine Sc during FIRE 87. [In this stationary regime, the other two datasets contribute one and two $E(k)$ points, respectively, which are highly uncertain, having only one or two k values per $E(k)$ value.] At the smallest scales (largest k), the energy densities show a remarkable agreement for all but the smoothest and longest dataset (14 July), which has $\approx 2^7 = 128$ times smaller $E(k)$. In the average spectrum (cf. Fig. 7), the contribution of this dataset is small: 4–8 times the weight but less than $1/100$ the energy ($1/10$ the amplitude). The three encapsulated points are affected by the 60-pixel glitch visible in Figs. 3c and 4a.

smaller β than smoothness (more energy in the mean and large scales). The observed variability of β is a good example of ergodicity violation, traceable in Fig. 6b to the large-scale (hence poorly sampled) behavior in each case. Clearly, five samples are not enough to estimate the natural range and relative frequency of $E(k)$, even for the restricted case of marine Sc; we will however attempt to estimate its mean in the next section.

The 14 July spectrum is worthy of a closer look, especially in the octave bin representation in Fig. 6b. First, we notice a small glitch in the scaling at abscissa ≈ 10 ($k \approx 2^{10}/L$ or $r \approx 2^6 = 64$ pixels); this is traceable to the anomalous dip discussed previously that is $\approx$60 pixels wide. Second, we see evidence of $E(k) \approx$ constant for abscissa $\leqslant 4$ ($k \leqslant 2^4/L$ hence scales $r \geqslant L/16 \approx 20$ km). We will return to this important phenomenon, visible also in the 30 June data and, to a lesser extent, in the 1717 16 July data in the following sections.

6. Exponents and scaling ranges for average LWC spectra from FIRE 87 and ASTEX

a. *The FIRE database: Comparison with structure function analysis*

Having focused on the striking differences between the various LWC time series and their β, we now examine their average properties. The first five rows in Table 2 summarize our results for β using the King datasets and a variety of regression and/or noise reduction techniques described and compared in appendix A. The entries in the last row are β values obtained by applying the same techniques to the ensemble-average spectrum, that is, the lower curve in Fig. 7a (which is not equivalent to averaging the individual exponents). This figure shows the average FIRE 87 spectrum for all King data in the standard representation using subsets with $N_p = 2^{13}$ points ($2^{12} = 4095$ k's) as well as with the 12 corresponding octavewide wavenumber bins. For the binning method, we find $\beta = 1.36 \pm 0.06$ with good scaling over more than three decades; as expected, the ensemble averaging reduces the uncertainty on β with respect to (most of) the individual cases. The scaling range goes from 10–20 m to 20–40 km. The 40-km (2^{13} point) limit is set simply so that each dataset contributes at least one datum at each scale; effectively, we are using 15 nonoverlapping sections of LWC data in this ensemble average.

We can better define the lower (η) and upper (R) limits of the scaling range with the help of the (second order) structure function, namely,

$$D(r) = \langle [\varphi(x + r) - \varphi(x)]^2 \rangle, \tag{4}$$

where the average is taken over space (x) and realizations (φ), in other words, the variance of the "increment" $\varphi(x + r) - \varphi(x)$. In theory, there is no new statistical information in $D(r)$, since it is in a Fourier-type duality with $E(k)$ (Weiner–Khinchine theorem). It can be shown that in the scaling range, $\eta \leqslant r \leqslant R$, we have

$$D(r) \propto r^{2H}, \tag{5a}$$

with

$$H = \frac{\beta - 1}{2} \quad (1 < \beta < 3) \tag{5b}$$

and another relation between the prefactors (e.g., Monin and Yaglom 1975). The exponent H cannot exceed 1, which translates (almost everywhere) differentiability in Eqs. (4) and (5a), nor become negative, since $H = 0$ expresses (almost everywhere) discontinuity—hence stationarity according to the classification presented in appendix B. In practice, however, $D(r)$ has advantages over $E(k)$: (i) it enables scale by scale analysis to go down to the pixel size $r = l$ (5 m

TABLE 2. Spectral exponents for FIRE 87 King LWC datasets, using different noise reduction and regression methods. The first estimate of β is obtained by dividing the N_{tot} points (see Table 1) into $N_s = 2$ subsets, computing their average spectrum, and using straightforward linear regression after taking logs in the scaling range. The next column is the result of computing spectra for $N_p = 512$ points at a time and averaging them over the number $N_s = [N_{tot}/N_p]$ of different realizations, as indicated in brackets. The last trio of columns use Eqs. (A3a) and (A3b) to obtain $E(k)$ at $[\log_2 N_{tot}] - 1$ different scales (k values) at roughly logarithmic intervals; those that fall in the scaling regime are used in a linear least squares regression. First, no weights are used (equivalently, $\sigma_{\log E}$ = const.); then the sum of squares is weighted by $1/\sigma^2_{\log E}$, as deduced from Eq. (A4a); finally, the dispersion in $\log k$ is also accounted for, according to Eq. (A4b). Entries in the last row correspond to the same methods but applied to the estimate of $E(k)$ using all the datasets, properly registered in k and weighted by the number of points used in computing each spectrum (namely, N_2 from Table 1).

Date (1987)	Time (UTC)	β No variance reduction	β (N_s) Method 1	β (method 2) No errors	Errors in E	Errors in k
30 June	2241	1.58	1.62 (56)	1.39 ± 0.03	1.38 ± 0.09	1.40 ± 0.03
2 July	0223	1.55	1.58 (32)	1.19 ± 0.04	1.10 ± 0.06	1.08 ± 0.07
14 July	2309	1.63	1.64 (128)	1.68 ± 0.04	1.67 ± 0.08	1.68 ± 0.04
16 July	1717	1.69	1.72 (16)	1.47 ± 0.05	1.50 ± 0.05	1.45 ± 0.08
16 July	1819	1.48	1.45 (23)	1.53 ± 0.04	1.49 ± 0.06	1.53 ± 0.08
Ensemble average		1.6	1.6 (255)	1.37 ± 0.03	1.38 ± 0.03	1.36 ± 0.06

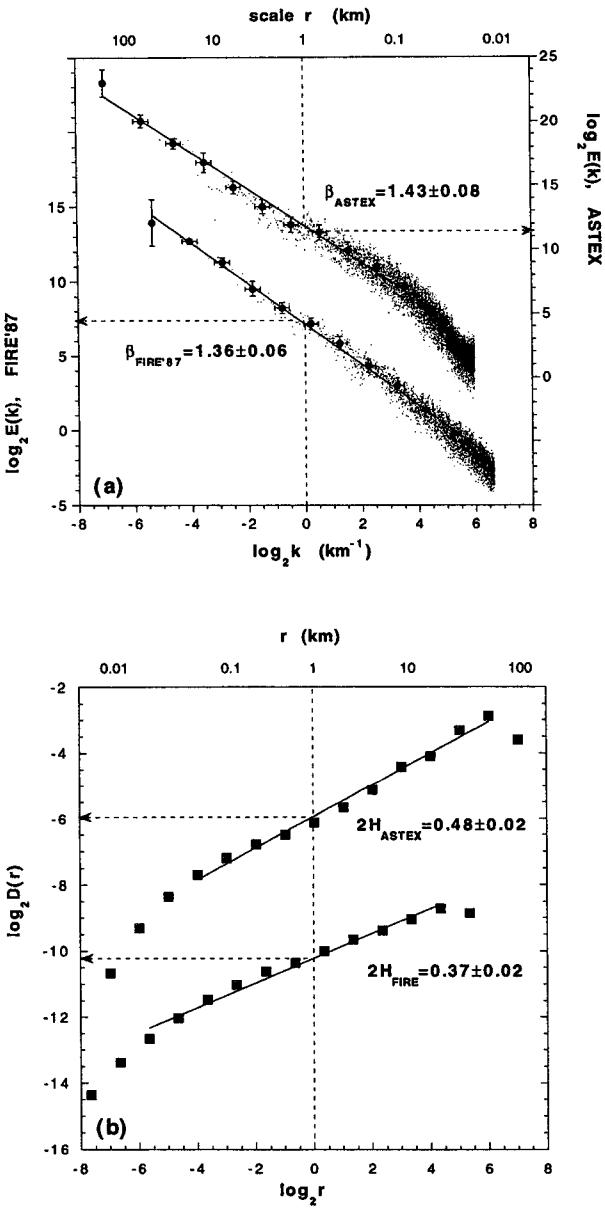

FIG. 7. Ensemble-average statistical properties for LWC in marine Sc for FIRE and ASTEX. (a) Energy spectra. The left axis and bottom curve refer to all five FIRE 87 spectra $E(k)$, weighted by their overall lengths L_2 determined from Table 1 and averaged prior to regression. Both the standard method (dust) and octave binning (bold dots) were used for wavenumbers sampled by all of the flights, even the shortest. The right axis and upper curve refer to five ASTEX datasets, described and analyzed by Davis et al. (1994a). The scale relevant to each wavenumber ($r = 1/k$) is indicated on the top axis. (b) Second-order structure functions: (bottom) FIRE 87; (upper) ASTEX. We have preliminary evidence for the anticipated scale break at the integral correlation scale: ~20 km for FIRE 87 and ~60 km for ASTEX.

here), as opposed to the inverse Nyquist frequency $2l$, and (ii) it spans a smaller range of values, due to the smaller numerical values of the exponent H with respect to β in Eq. (5b). Thus, $D(r)$ provides a better baseline for the scaling and is less forgiving with deviations from power-law behavior, hence more sensitive to scale breaks. [The disadvantage of $D(r)$ becomes apparent in higher dimensions; being essentially a convolution product, it is impractical to compute it in physical space.]

The results for $D(r)$ presented in log–log axes in Fig. 7b support $\eta \approx 4l = 20$ m for the lower end of the scaling range. At the upper end, transition to a flat structure function is observed at 20–40 km. This is to be expected at the integral scale, R, of a process; to a first approximation, the data is correlated at scales $r < R$ and uncorrelated beyond, hence the scale-independent increments (cf. appendix B for an example). So the structure functions in Fig. 7b support $R \approx 20$ km for this database. Between these two limits, we find a slope of $2H = 0.37 \pm 0.02$, which is compatible with $\beta - 1$ as expected from Eq. (5b); this would not be the case if we relied only on the noise reduction and regression techniques dominated by large k values (leading to $\beta \approx 1.6$, cf. appendix A).

At any rate, the interval $[\eta, R]$ includes both the cloud (200–400 m) and boundary layer thicknesses ($\lesssim$1 km), which roughly coincides with the altitude of the relatively well-defined cloud top in the case of marine Sc. Both these scales control thermo- and hydrodynamical processes unfolding largely in the vertical, apparently, they do not directly affect the mechanisms that distribute LWC horizontally in these highly stratified systems. Neither is there any evidence of a scale break around 200 m in the LWC, as is observed in Landsat radiance fields emerging from marine Sc (Cahalan and Snider 1989; Lovejoy et al. 1993); this decoupling of the cloud's apparent and inherent structures is explained by Davis et al. (1996, submitted to *J. Atmos. Sci.*) in purely radiative terms.

b. A comparison with ASTEX data and Kolmogorov scaling

For comparison, Fig. 7a reproduces Davis et al.'s (1994a) $E(k)$ for transects of LWC obtained inside marine Sc during ASTEX with a PVM-100 probe (Gerber et al. 1994), their spectral data being extended here to twice larger scales. Five datasets were used, all $2^{14} = 16\,384$ points long, sampled at 10 Hz with aircraft speed ~80 m s^{-1} (overall length $L \approx 130$ km and resolution $l \approx 8$ m). The spectral exponent (for octave bins) is $\beta_{ASTEX} = 1.43 \pm 0.8$, not far from β_{FIRE}; the observed scaling range, however, is clearly shifted. The (second order) structure function results of Davis et al. are reproduced also, in Fig. 7b showing $\eta \approx 60$ m as the beginning of the scaling range and preliminary evidence that the integral scale $R_{ASTEX} \approx 60$ km. The structure function exponent $2H$ is 0.48 ± 0.02 for ASTEX, again in numerical agreement with β in Eq. (5b).

For ASTEX more than for FIRE 87 spectral data, we see evidence of a steeper spectrum at scales smaller

than $\eta \approx 60$ m and a hint of white noise contamination, probably of instrumental origin, at the very smallest scales $\sim 2l$. In contrast with the J–W hot-wire probe (cf. section 4), the steeper spectrum is not due to an artificial smoothing caused by an oversampling of the output of an instrument too slow to respond to natural variability; indeed, the PVM-100 probe can take data at 2 kHz ($\sim$5 cm resolution) without oversampling. We suspect that the presence of a few large jumps in the LWC record at scales $\leqslant \eta$, a natural consequence of intermittency, causes a smooth transition toward scaling in k^{-2}.

For two processes with $E(k) \propto k^{-\beta}$ having similar exponents and prefactors (intercepts on $\log E$ axis) but different scaling ranges, the one with the largest scales—ASTEX in this case—will have the larger variability. Judging by the variance levels at $r = 1$ km ($k = 1$ km^{-1}) in Figs. 7a and 7b, we see that ASTEX fluctuations are more intense than those of FIRE 87 at this scale by a factor of $\sim 2^4$ in energy and $\sim 2^2$ in amplitude. This ratio would lead to negative LWC values if the mean were not boosted proportionately, and, indeed, LWC values >1 g m^{-3} were not rare in ASTEX clouds (Davis et al. 1994a). These differences are probably due to the boundary layer being at least twice as deep in ASTEX as during FIRE 87, but there may be other causes as well.

In short, we can think of marine Sc in ASTEX as a scaled-up version of those observed during FIRE 87. This scaling-up considerably affects the range of scales involved, the levels of LWC, and its overall variance but not so much the exponents β and H. This argues for a degree of universality in the complex coupled thermodynamical and hydrodynamical mechanisms that determine the internal structure of marine Sc. The similarity in scaling properties means that the cloud size, mean LWC, and its overall variance depend strongly on the local climatological conditions, and on the way in which the LWC is distributed inside the clouds only weakly.

Finally, we conclude from an examination of our β values that LWC in marine Sc do not, in general, follow a (Kolmogorov 1941) "$-5/3$" law, as predicted for velocity by the (down-scale energy) cascade phenomenology in fully developed, homogeneous and isotropic 3D turbulence and generalized to the density fluctuations for a passive admixture (Obukhov 1949; Corrsin 1951). A $5/3$ exponent is also obtained for (up-scale enstrophy) cascades in 2D turbulence (Kraichnan 1967). However, $5/3$ is not within even the most generous error bars on any of our estimates of β in Table 2, except for the relatively smooth 14 July case.

7. Stationarity and continuity in LWC fields

It is easy to see why there must be an upper bound R to the scaling range for any physical process with $E(k) \propto k^{-\beta}$ and $\beta > 1$. Such processes have finite "energy" (variance) in any wavenumber interval $[k_{\min}, \infty)$, but as $k_{\min} \to 0$, we get arbitrarily large amounts of energy cumulating in the large scales. This so-called infrared catastrophe is avoided by a transition to $E(k) \approx$ constant for $k < 1/R$, where R is integral scale. If furthermore the variable is, like LWC, nonnegative, then the amplitude ($\propto \sqrt{E(k)}$) of its fluctuations must level off at the scale for which it reaches the mean; otherwise, negative values will occur. This is precisely what we observed in some individual LWC spectra (Fig. 6b) and in the ensemble-average structure functions (Fig. 7b).

In appendix B, we relate the scaling of the energy spectrum to important properties: stationarity (statistical invariance under translation) and stochastic continuity (neighboring data points likely to have close values), noting that both are tangible descriptions of variability, being defined in physical, rather than in Fourier, space. Both stationarity and scaling are essentially symmetries possessed by some datasets and not by others. When asking about scaling, we compare the properties of small and large portions of data (e.g., in the product $\varphi(x + r)\varphi(x)$, we change the scale parameter r); for stationarity, we compare different parts of equal size (e.g., in $\varphi(x + r)\varphi(x)$, we change the position parameter x). Stationarity is critically important because it is a prerequisite for obtaining meaningful spatial statistics. Stochastic continuity is an issue of correlation between neighboring points; if, for a small separation r, $\varphi(x + r)$ and $\varphi(x)$ are highly correlated, then the increment $|\varphi(x + r) - \varphi(x)|$ is generally small, and the data is stochastically continuous; if the same increment is generally large, then the data is discontinuous.

The arguments presented in appendix B tell us that atmospheric processes with $\beta < 1$ can be classified as stationary and discontinuous whereas those with $\beta > 1$ are nonstationary per se but have continuity; if $\beta < 3$, the increments $\varphi(x + r) - \varphi(x)$ are stationary. The integral scale R that separates scales where $\beta \approx 0$ from those where $\beta \approx 1.5$ (for LWC) thus defines the threshold between large-scale stationary and small-scale nonstationary regimes. In terms of continuity, LWC values are highly correlated at scales $\ll R$ and essentially uncorrelated at scales $\gg R$.

Figures 8a and 8b illustrate the effect of long-range correlations in LWC, up to $R \approx 20$–40 km, on the running estimates of the mean $m_\varphi(r, x)$ and standard deviation $\sigma_\varphi(r, x)$ in Eqs. (3a) and (3b). Panel a shows $m_\varphi(r, x)$ versus r for 15 nonoverlapping intervals, each 2^{13} points (41 km) long in our database (41 km is the length of the shortest dataset). To a first approximation, the running means are unstable for $0 < r < 20$ km and tend to level off for 20 km $< r <$ 40 km, albeit at different levels between $\langle \text{LWC} \rangle \pm \sigma_{\text{LWC}}$ (except for one). Figure 8b shows the 15 independent estimates of $\sigma_\varphi(r, x)$ versus r, in log–log axes. In most, but not all cases, $\sigma_\varphi(r, x)$ tends to increase with r, often by jumps.

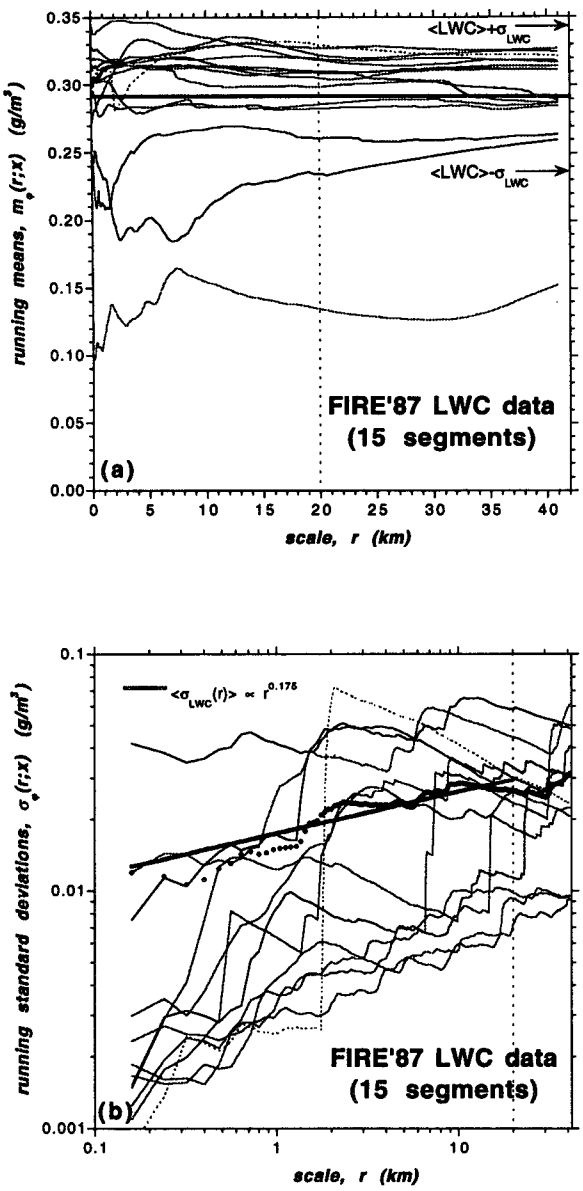

FIG. 8. Gaussian statistics of LWC as a function of scale r and realization, revisited. (a) As in Fig. 5a but for independent running means $m_\varphi(r, x)$, that is, taken from different datasets and/or starting at positions x separated by the maximal r value, 2^{13} points (~41 km). The effect of correlations on $m_\varphi(r, x)$ does not subside until r exceeds at least 20 km. The ensemble-mean ⟨LWC⟩ and standard deviation, $\pm\sigma_{\mathrm{LWC}}$, are also indicated. (b) As in (a) but for running standard deviations $\sigma_\varphi(r, x)$ in log–log axes. The x, φ average of the $\sigma_\varphi(r, x)$'s, excluding the fifth portion of the 14 July flight (dotted line) that contains the glitch in Figs. 3c and 2a follows the anticipated scaling in r^H (where $2H = \beta - 1 = 0.36 \pm 0.03$) at least up to $r \approx 20$ km.

The most dramatic jump occurs for the anomalous 14 July (7/14) case; as r increases, $\sigma_{7/14}(r, 4 \times 2^{13}l)$ goes from the minimum in the group of 15 to the maximum value. Even excluding this realization, there is considerable case to case variability and more so at small values of r than large. The root-mean-square (rms) ensemble average of the 14 remaining cases has been overlaid in Fig. 8b. The rms $\sigma_\varphi(r, x)$ is well approximated empirically by a power law in r with an exponent ~ 0.175 for r less than 20 km. This is not surprising since scaling arguments tell us that rms $\sigma_\varphi(r, x)$ should go as the square root of the second-order structure function in Eq. (5a); hence, $r^H \approx r^{0.18}$.

With β ranging from ~1.2 to ~1.7 for octave-binned $E(k)$, the LWC fields $\varphi_i (i = 0, \cdots, N)$, partially illustrated in Figs. 3a–e, are nonstationary per se, and the problems evoked in connection with Figs. 5a and 5b and 8a and 8b follow. However, we can focus on the stationary features of this data: either increments $\varphi_i - \varphi_{i-r}$ $(r > 0, i = r, \cdots, N)$ or the gradient field $\varphi_i - \varphi_{i-1}$ $(i = 1, \cdots, N)$. For these gradient fields $(\beta \to \beta - 2)$, we would find spectral exponents in the (stationary) range: $[1.2, 1.7] \to [-0.8, -0.3]$. Figure 9a shows φ_i taken from the second 2^{13} point section of the 30 June LWC dataset (the first section of which is shown in Fig. 1a); Fig. 9b shows the corresponding absolute gradient field $\epsilon_i = |\varphi_i - \varphi_{i-1}|$ $(i = 1, \cdots, N)$. Figure 10 shows $E(k)$ for the five LWC absolute gradient fields. Because the absolute value operation suppresses high frequencies, the spectral exponents occupy a narrower positive range [0.5, 0.8], and the ensemble-average spectrum yields $\beta = 0.7$. Since these spectral exponents are <1, gradient fields are stationary.

This classification conflicts somewhat with the conventional wisdom about statistical stationarity. The gradient fields have transient behavior (sudden strong deviations from the background level) and broad variability (maximum/minimum ratios ≈ 100 for datasets only a few thousand pixel point long); both of these characteristics are commonly viewed as symptoms of nonstationarity. However, scale invariance implies discontinuity in stationary regimes and a priori allows for arbitrarily large jumps. Implicit in using only first- and second-order statistics is a (generally unjustified) Gaussian assumption, which implies that strong deviations are very unlikely.

8. Summary and discussion

a. Scale invariance of LWC distributions

Using aircraft data obtained during FIRE 87, we have established that horizontal transects through LWC fields in marine Sc exhibit power-law spectra, $E(k) \propto k^{-\beta}$, over scales from 20 m to at least 20 km. This is one of many possible signatures of statistical scale invariance. We find $\beta = 1.36 \pm 0.06$ for the average over five datasets collected with the King probe and a considerable range, 1.1–1.7, going from case to case (Table 2). Two other LWC instruments were used, an FSSP and a Johnson–Williams probe, but their outputs show major deviations from scale invariance as a consequence of well-documented instrumental shortcomings, compare section 4.

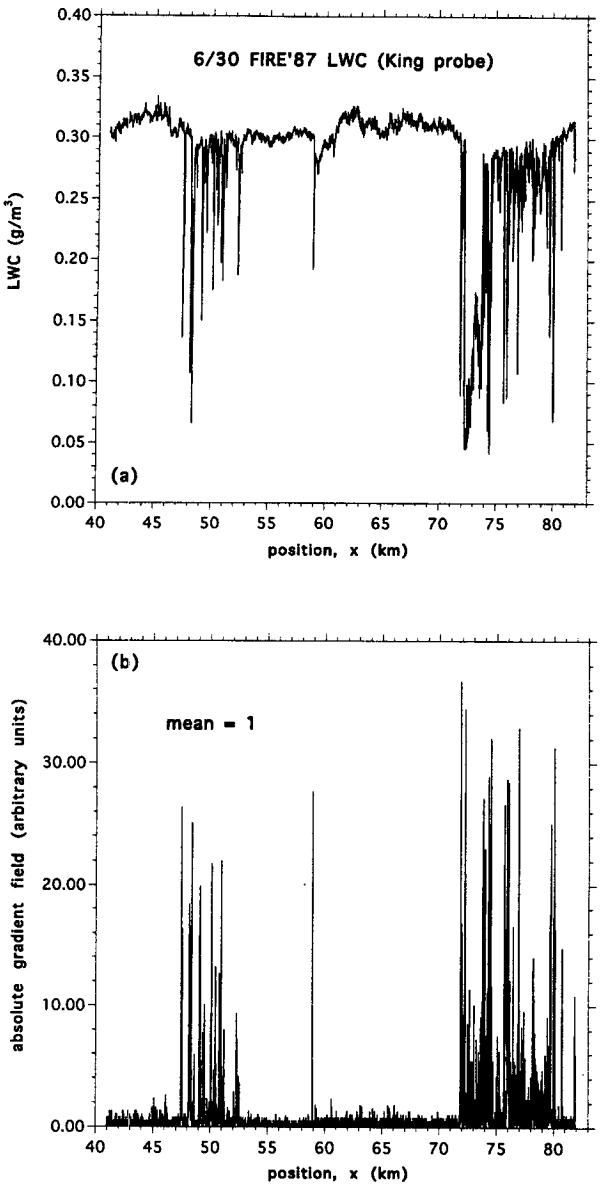

FIG. 9. More FIRE 87 LWC data and the associated small-scale absolute gradient field. (a) Second 41-km long segment of the 30 June LWC data, an example of a nonstationary data stream with intermittent bursts of activity. (b) Next-neighbor absolute differences of the data in (a), normalized to unity, an example of a stationary but highly intermittent data stream.

It may seem surprising that a collection of LWC transects as visually disparate as those of FIRE 87 (Figs. 3a–e and Table 1) and/or ASTEX (figures in Davis et al. 1994a) can yield, as a whole, such simple spectra as the two in Fig. 7. This figure is nonetheless a robust statement about the statistical scale invariance of LWC fluctuations in marine Sc. In conjunction with information about stratification, both the ensemble-average scaling and its flight to flight variability strongly constrain future modeling of internal marine Sc structure, both dynamic and stochastic. An important application of the latter type is to provide input into 3D radiative transfer code (e.g., Cahalan et al. 1994a,b).

Another surprise is that within the scaling range there are two scales widely believed to be important in the vertical structure of marine Sc decks: the cloud thickness (200–400 m) and the boundary layer thickness ($\leqslant$1 km). We find neither is a scale break in LWC fluctuations at $\approx$200 m where Cahalan and Snider (1989) and others found one in Landsat radiance fields from marine Sc scenes captured during FIRE 87, going from a $\beta \approx 5/3$ scaling to a steeper trend (smoother behavior) at smaller scales; for more details, see Davis et al. (1996, submitted to *J. Atmos. Sci.*).

The spectral properties of large unbroken ASTEX clouds are both similar to and different from those of FIRE 87. The spectral exponent $\beta = 1.43 \pm 0.08$ is not far from that in FIRE 87, and the scaling range also spans three orders of magnitude; this argues for a degree of universality in the processes that shape marine Sc under different climatological conditions. However, the scaling range is shifted upward by a factor of $\approx$3 (from 60 m to over 60 km), and LWC means and fluctuations are shifted upward by a similar factor. Both shifts are probably due to the more vigorous dynamics in the ASTEX boundary layer, which was at least twice as thick as that in FIRE 87.

b. Nonstationarity

In data analysis, our need for *stationary* quantities is so fundamental that stationarity is usually taken for granted. This is however a dangerous practice. Many commonly used statistical procedures produce at best ambiguous and at worst meaningless results for nonsta-

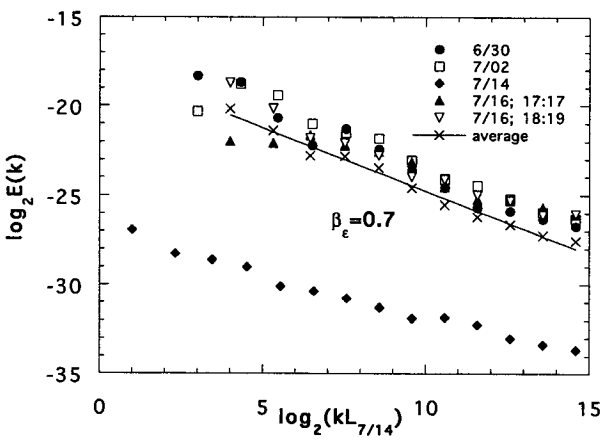

FIG. 10. Individual and average energy spectra for absolute gradients in LWC for FIRE 87. As in Figs. 6b and 7a but for the absolute next-neighbor difference fields, as in Figs. 9b but for all the data. This illustrates stationarity (with intermittency) in scale-invariant data: $E(k) \sim k^{-\beta}$ with $\beta < 1$ (in the range 0.5–0.8 in this case).

tionary data. For instance, we have shown how, in LWC datasets shorter than 20–40 km, means and variances have little if any meaning, because at these scales the data are nonstationary. By combining scaling concepts and spectral analysis, we can classify atmospheric data as stationary or not and, more importantly, determine the range of scales where these attributes apply.

There are two broad categories of stochastic processes and/or datasets $\varphi(x)$ with $E(k) \propto k^{-\beta}$: $\beta < 1$, which is stationary with stochastic discontinuity, hence relatively short range correlations, and $\beta > 1$, which is nonstationary per se but stochastically continuous, hence long-range correlations. This simple way of assessing the stationarity of a time series has been previously overlooked in favor of more complex procedures in physical space that generally focus on some specific scales and are therefore somewhat ad hoc.

We note that nonstationarity is ubiquitous but not a difficult situation to handle. In many cases (including LWC), we have $1 < \beta < 3$; then increments (over distances falling within the scaling range) are stationary and only these should be the focus of averaging procedures in physical space. We can have both stationary and nonstationary behavior in a single dataset but necessarily within different scaling ranges, generally large-scale stationarity and small-scale nonstationarity with a transition at the integral scale, which we tentatively set at ≈20 km for FIRE 87 and ≈60 km for ASTEX.

c. *Need for analyses beyond energy spectra*

It is important to not overemphasize one particular statistic. In the case of spectral analysis, we have underscored its usefulness in distinguishing and measuring stationary and nonstationary scale-invariant regimes. However, we must bear in mind that very different looking random processes can have similar $E(k)$. For instance, Gaussian white noises and randomly positioned Dirac δ functions both have flat ($\beta = 0$) spectra; their integrals, Brownian motion and randomly positioned Heaviside steps, both have scaling spectra with $\beta = 2$; LWC fluctuations have negatively skewed pdf's, while Mandelbrot's (1977) fractional Brownian motions are symmetric, yet its spectrum can be made identical to LWC's. This inherent ambiguity of spectral analysis can be resolved only by using more general approaches such as those described by Davis et al. (1994a,b) and in the sequel of this study.

Our main motivation for performing statistical analyses of LWC is to constrain new and improved stochastic models of cloud structure, which can, in turn, be used to simulate cloud radiative transfer. For this application, the longest possible datasets with the widest possible range of scales is needed. At the smallest scales, Baker (1992) has found much stronger variability in droplet concentration at centimeter to meter scales than anyone previously suspected. If this variability is strong enough, it could modify the exponential extinction law that underlies all of current radiative transfer theory (Davis 1992). At the largest scales, we have seen that we cannot trust even the simplest statistics, like running means, unless taken over at least an integral scale, which means, at a bare minimum, ≈20 km for marine Sc off California and ≈60 km for marine Sc around the Azores. Thus, we need liquid water datasets at least ≈100-km long, with resolution down to meters or even centimeters, to properly inform cloud radiative transfer modeling. So far, we have barely scratched the surface in acquiring and analyzing such datasets, and we are far from having any good climatology of liquid water in clouds.

Acknowledgments. This work was supported by the Environmental Sciences Division of U.S. Department of Energy (under Grant DE-A105-90ER61069 to NASA's Goddard Space Flight Center) as part of the Atmospheric Radiation Measurement (ARM) program. We are grateful to Drs. Phil Austin, M. King, and T. Arnold for giving us access to the FIRE archives. We thank them and M. Baker, B. Baker, J.-L. Brenguier, C. Duroure, H. Gerber, S. Malinowski, R. Pincus, and T. Warn for fruitful discussions, and the more or less anonymous reviewers for their helpful comments.

APPENDIX A

Spectral Noise Reduction and Exponent Determination

We address here the problem of reducing the statistical noise in FFT-based estimators of $E(k)$ and the related issue of using regressions to determine the exponent β in $E(k) \sim 1/k^{\beta}$.

a. *Discrete Fourier transform and spectral estimation*

In a realistic data analysis situation, we generally have only a small number of realizations or experiments with a finite spatial sampling, assumed uniform:

$$\varphi(x_i),\ x_i = il\ (i = 1, \cdots, N_{\text{tot}}), \qquad \text{(A1a)}$$

where $N_{\text{tot}} = L/l$ is the total number of points, L the spatial length of record, and l the step size. For our LWC data, we have entered N_{tot} and L in Table 1, l being approximately 5 m (sampling rate 20 Hz and aircraft velocity ≈ 100 m s^{-1}). The discrete Fourier transform of the data in Eq. (A1a) is denoted by

$$\tilde{\varphi}(\pm k_j), \quad \pm k_j = \frac{\pm j}{L_2} \quad \left(j = 0, \cdots, \frac{N_2}{2}\right), \qquad \text{(A1b)}$$

where $N_2 = 2^{[\log_2 N_{\text{tot}}]}$ is the largest integer power of two less than N_{tot} ($[\cdot]$ designates integer part) and $L_2 = N_2 l$. The associated energy density is

$$E(k_j) = \frac{2}{L_2} |\tilde{\varphi}(k_j)|^2 \quad \left(j = 1, \cdots, \frac{N_2}{2} - 1\right), \quad \text{(A2)}$$

since $\tilde{\varphi}(-k_j) = \tilde{\varphi}(k_j)^*$ for real data in Eq. (1). Note that we are not concerned with $E(k_j)$ at the Nyquist frequency (at $j = N_2/2$) nor the origin component (at $j = 0$) in the following.

Ensemble averages call for special care. The natural unit for x in Eq. (A1a) is $\Delta x = l$, whereas its counterpart for k in Eq. (A1b) is $\Delta k = 1/L_2$. In our case, the realizations have different L_2's and equal sampling scale l, but different l's can also occur. In all cases, we must adopt common units for the wavenumber sequences when comparing and averaging spectra. (We took $\Delta k = 1/L_{2,\max}$ where $L_{2,\max} = 2^{16}l \approx 328$ km for the 14 July data.) Then, as required implicitly by Eq. (1), we cumulate $E(k)L_2 \propto E(k)N_2$ in bins of width Δk.

We now compare different methods of estimating $E(k)$ from a single dataset and discuss their advantages and disadvantages.

b. Statistical noise reduction

When dealing with a single dataset with N_{tot} points rather than an ensemble, we simply drop the angle brackets in Eq. (1) and assume this will give us a reasonable estimate of the spectrum. The standard deviation of this single-run estimate of $E(k)$ is however equal to its mean (Press et al. 1993). This large statistical noise can be reduced by subdividing the dataset into a number $N_s = N_{\text{tot}}/N_p$ of subsets of N_p points each; each chunk of data is viewed as a different realization. Then the spectrum for each subset is computed, and the results are averaged over the N_s subsets with empirical variances associated to each $E(k)$ (noise reduction method 1). The cost of this noise reducing procedure is loss of information at the large scales (low wavenumbers): k now goes from $k_{\min} = N_s/L$ to $k_{\max} = 1/(2l)$. To implement this method, we used Press et al.'s routine SPCTRM, which allows for $N_s \geqslant 2$.

In the above estimation of $E(k)$, not only is some large-scale information lost in favor of noise reduction, but a least squares fit to the power-law form in Eq. (2) on a $\log E$ versus $\log k$ plot will be dominated by the smallest of the remaining scales (largest wavenumbers). The contribution of large scales to the exponent β becomes virtually nil. To make all scales contribute equally, we propose to average $E(k)$ by octaves, that is, factors of 2 in k (noise reduction method 2). Temporarily adopting units where $L_2 = 1$ in Eqs. (A1b) and (A2), we create a sequence of wavenumber bins of increasing size 2^m ($m = 0, \cdots, [\log_2 N_{\text{tot}}] - 2$) and compute an energy estimate for each bin:

$$\bar{E}_m = \frac{1}{2^m} \sum_{j=2^m}^{2^{m+1}-1} E(k_j), \quad \text{(A3a)}$$

corresponding to average wavenumbers,

$$\bar{k}_m = \frac{1}{2^m} \sum_{j=2^m}^{2^{m+1}-1} k_j = \frac{3}{2} 2^m - \frac{1}{2}, \quad \text{(A3b)}$$

which are equally spaced on a log scale only in the limit $m \gg 1$. We thus obtain exactly $[\log_2 N_{\text{tot}}] - 1$ estimates for $E(k)$. Clearly, the small-scale (large m) estimates will be more reliable than their large-scale (small m) counterparts, which suffer from small number statistics. However, this is a fundamental limitation of data analysis, remedied only by acquiring a longer dataset and/or more datasets of the same length. Noise reduction methods 1 (subdivision) and 2 (octave binning) can of course be combined, leading to $[\log_2 N_p] - 1$ improved estimates of $E(k)$.

For future needs, we also compute the variances

$$\text{var}[E]_m = \begin{cases} E(k_1)^2, & m = 0 \\ \dfrac{1}{1 - 2^{-m}} \left[\dfrac{1}{2^m} \displaystyle\sum_{j=2^m}^{2^{m+1}-1} E(k_j)^2 - \bar{E}_m^2 \right], & m > 0 \end{cases} \quad \text{(A4a)}$$

and

$$\text{var}[k]_m = \frac{1}{2^m} \sum_{j=2^m}^{2^{m+1}-1} k_j^2 - \bar{k}_m^2 = \frac{2^{2m-1} - 1}{12}, \quad \text{(A4b)}$$

from which we deduce standard deviations σ_E and σ_k and their counterparts for $\log E$ and $\log k$.

c. Exponent estimation

We now wish to estimate β in Eq. (2) and determine the range of scales over which the power law applies, the scaling range, which need not encompass all the observed scales (l to L). Numerous methods for finding exponents have been described in connection with many different types of scaling statistics. Transposed into our notations, the most popular methods are

- plotting $E(k)k^\beta$ versus k for a number of "test" values of β, seeking the one that remains the most constant in the scaling range;
- plotting $\Delta \log E(k)/(-\Delta \log k)$, a "local" value of β, versus k and estimating β as its mean over the scaling range;
- a nonlinear least squares regression to fit the $E(k)$ data with the two parameters in $Ak^{-\beta}$; or
- a linear regression of $\log E(k)$ in $A - \beta \log k$.

This last procedure is the easiest to implement and automate and therefore the most used. However, using a linear regression in the logs introduces, in principle, a bias, but latter we show this bias is negligible when the scaling is good (lines in the log–log plots are straight).

In the restricted framework of linear regression methods alone, there are still different strategies: k-dependent variances can be optionally assigned to either

the $\log E(k)$ axis only or to both axes, compare Eqs. (A4a) and (A4b). In the former case, we can use any program that computes the coefficients A and B that minimize the weighted sum of n squares, $\chi^2(A, B) = \Sigma_1^n (A + Bx_i - y_i)^2/\sigma_{yi}^2$, for instance, Press et al.'s (1993) routine FIT. In the latter case, we use their routine FITEXY that minimizes $\Sigma_1^n (A + Bx_i - y_i)^2/(\sigma_{yi}^2 + B^2\sigma_{xi}^2)$. FIT and FITEXY return estimates of the uncertainties in A (the prefactor) and B (the exponent, $-\beta$); the latter are used below whenever we write $\beta \pm \delta\beta$.

d. Method comparisons

Various estimations of $E(k)$ described in appendix A(b) are illustrated with the King 2 July data, one of the most complex cases (2^{14} = 16 384 points long, half of which are graphed in Fig. 3b), keeping the regression method constant. For simplicity, we use an unweighted linear least squares fit in logs, the kind of regression that is done by typical plotting applications for desktop computers. Figure A1, a plot of $\log E(k)$ versus $\log k$, shows how similar exponents $\beta \approx 1.56$ for both no noise reduction and method 1 ($N_s = 32$ subdividing) are. The regression lines are controlled mainly by the small-scale (large k) points due to their large density on the logarithmic axis, traceable to the linear discretization of k space. These slopes are hard to distinguish visually from $5/3$ (the lowest line). In contrast, method 2 (octave binning) yields a noticeably smaller slope ≈ 1.19 with a better fit over the full range of scales.

In Fig. A2, we show only $\log\bar{E}_m$ versus $\log\bar{k}_m$ ($m = 0, \cdots, 12$) from Eqs. (A3a) and (A3b) for the same dataset, with error bars deduced from Eqs. (A4a) and (A4b). The four regression lines correspond to three linear regressions and a nonlinear one. Nonlinear regression of $\bar{E}_m$ to $A\bar{k}_m^{-\beta}$ yields $\beta = 1.12 \pm 0.07$, when $\sigma_{E,m}$ is obtained empirically from Eq. (A4a), whereas, using a priori estimates $\sigma_{E,m} = \bar{E}_m$, we find $\beta = 1.18 \pm 0.09$ (not indicated in the figure). Turning to linear regressions, we find $\beta = 1.19 \pm 0.04$ in the simplest case (hold $\sigma_{\log E,m}$ constant and neglect $\sigma_{\log k,m}$), so the bias in β due to using logs is small. Using Eqs. (A3a) and (A4a) to obtain $\sigma_{\log E,m}$ and neglecting $\sigma_{\log k,m}$ yields 1.10 ± 0.06. Finally, accounting for the dependence of $\sigma_{\log k,m}$ on m in Eq. (A4b) leads to $\beta = 1.08 \pm 0.07$.

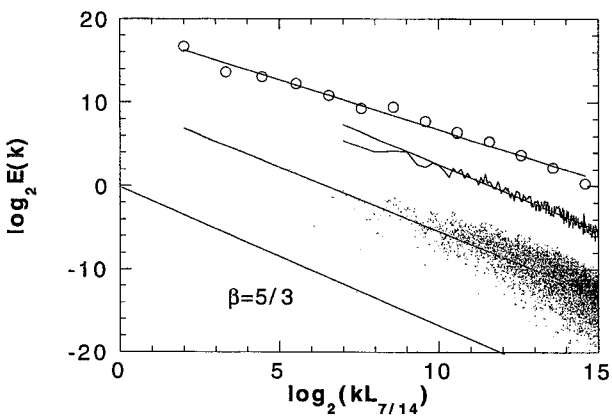

FIG. A1. Energy spectra for LWC in marine Sc, using different estimators for the 2 July 1987 King robe data. In these FFT-based computations, Press et al.'s (1993) subroutine SPCTRM is invoked for wavenumbers ranging from $k_{\min} = N_s/L_2$, with $N_s \geqslant 2$, to the Nyquist frequency, namely, $k_{\max} = 1/(2l)$. From bottom to top: $k^{-5/3}$, for reference; followed by the standard method (averaging over $N_s = N_{\text{tot}}/N_p$ subsets, $N_{\text{tot}} = 2^{14}$), with $N_s = 2$ ($k_{\min} = 2/L_2$) first, then $N_s = 32$ ($k_{\min} = 2^5/L_2$) for better variance reduction; followed by the 12 octave-wide bins needed to accommodate the former case. Vertical displacement is used for clarity in this log–log plot.

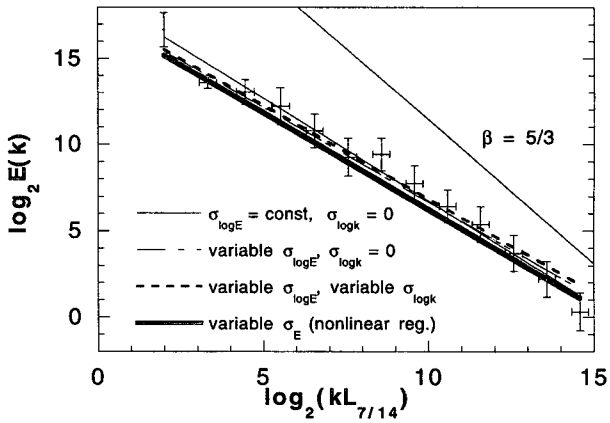

FIG. A2. Different regression methods for $E(k)$ vs k illustrated with 2 July 1987 LWC King data. The 13 data points correspond to the octave-wide wavenumber bins for the 2 July time series. Four different regressions are performed on this spectral data. The nonlinear regression of $E(k)$ to $Ak^{-\beta}$ is indicated in bold, yielding $\beta = 1.12 \pm 0.07$. The three others are linear regressions of $\log E(k)$ to $A - \beta \log k$: without any error bars ($\beta = 1.19 \pm 0.04$), with error bars in E only ($\beta = 1.10 \pm 0.06$), and with error bars in both E and k ($\beta = 1.08 \pm 0.07$).

e. Summary

Using a single dataset, we obtain values of β ranging from almost 1.6 for the most simplistic fitting technique and the most standard representation of $E(k)$ to 1.2 for octave-binned $E(k)$ and to 1.1 when using furthermore either a nonlinear regression or a sophisticated linear one. Results for all five King datasets are presented in Table 2, showing that the 2 July case used here has the largest exponent discrepancies and uncertainties. We conclude that (i) octave binning is a reasonable resolution of the dilemma between spectral noise reduction and loss of large-scale information and (ii) for exponent determination, straightforward linear regression in log–log axes is sufficient, at least for our applications.

APPENDIX B

Statistical Stationarity and Stochastic Continuity in Scale-Invariant Data

We explore here the consequences in physical space of scaling in Fourier space. Explicitly, we discuss statistical stationarity and stochastic continuity, and their relation to each other and to spectral properties in the framework of scale invariance. The key issue of stationarity is widely ignored in analyzing atmospheric data, but it is perilous to do so. Even the simplest statistical properties (such as variances and autocorrelations) become at best ambiguous and at worst meaningless if the data are nonstationary.

a. Stationarity and continuity: A second-order statistical perspective

We are interested in the statistically well-defined properties of a particular realization $\varphi(x)$ of some atmospheric time series or transect of a field. One of these is its pdf or one-point distribution, which views $\varphi(x)$ merely as a sequence of independent random numbers, their order being irrelevant. However, the values of $\varphi(x)$ are generally not independent, with one notable exception: white noise (cf. Fig. B1). To detect the correlations in the data, we must use two-point statistics at least, the most popular in time series analysis being the autocorrelation function:

$$\langle \varphi(x)\varphi(x+r)\rangle = G(r,x) \equiv G(r) \qquad \text{(B1)}$$

in situations where $\langle \varphi(x)\rangle \equiv 0$. The identity in Eq. (B1) applies only for "stationary" processes. The general, so-called narrow sense, definition of stationarity is statistical invariance under x translation of all n-point statistics; the so-called broad sense definition uses only $\langle \varphi(x)\varphi(x+r)\rangle$ and is sufficient for our present purposes.

Another property of interest is "stochastic continuity," meaning that (e.g., Papoulis 1965)

$$\langle [\varphi(x+r) - \varphi(x)]^2\rangle \to 0 \quad \text{as} \quad |r| \to 0. \qquad \text{(B2)}$$

If stationarity prevails, then

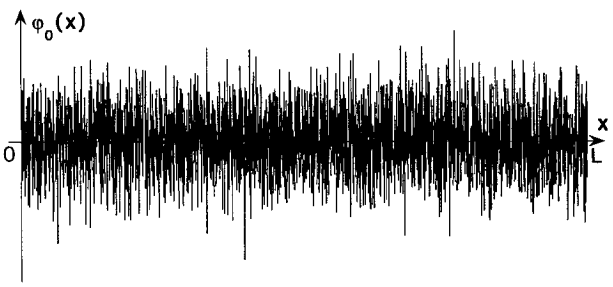

FIG. B1. White noise: an example of statistical scale invariance with stationarity and discontinuity. A total of 4096 uncorrelated random numbers drawn from a Gaussian distribution with zero mean; viewed as a time-series, the spectral exponent is $\beta = 0$.

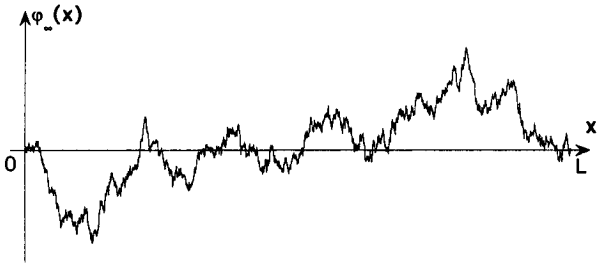

FIG. B2. Brownian motion: an example of statistical scale invariance with nonstationarity and continuity. Integral of the data in Fig. B1; the spectral exponent is now $\beta = 2$. In sharp contrast with the white noise in Fig. B1, zero crossing is a rare occurrence; the set $\{x > 0, \varphi_\infty(x) = 0\}$ is very sparse, its fractal dimension being only 1/2 (Falconer 1990). This illustrates how infrequently nonstationary processes take on typical (i.e., most probable) values due to their propensity to slowly wander off to $\pm\infty$.

$$\langle [\varphi(x+r) - \varphi(x)]^2\rangle = 2[G(0) - G(r)], \qquad \text{(B3)}$$

so $\varphi(x)$ is stochastically continuous if $G(r)$ is continuous at $r = 0$. We illustrate (non)stationarity and (dis)continuity with three examples.

1) White noise, a sequence of independent random numbers, is the simplest stochastic process. It is stationary and stochastically discontinuous because

$$G(r) \propto \delta(r). \qquad \text{(B4)}$$

It has trivial statistics beyond its one-point pdf; Fig. B1 gives a realization using normally distributed deviates with zero mean, so its pdf is Gaussian by construction.

2) Brownian motion, the next simplest example, is just the integral of white noise. The realization illustrated in Fig. B2 is the running sum of the data in Fig. B1, starting at $x = 0$ with $\varphi(0) = 0$. This assumption makes the origin a special point. The pdf is again Gaussian; its one-point variance $\langle \varphi(x)^2\rangle$ is, however,

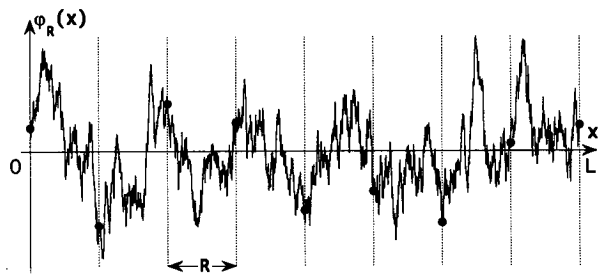

FIG. B3. Ornstein–Uhlenbeck process: continuous and stationary but nonscaling. Intervals of length $R = L/8$, the integral correlation scale, are clearly indicated; the process exhibits a statistical "periodicity" in the sense that each "period" of length R is uncorrelated with the others. We have $E_R(k) \propto 1/[1 + (2\pi kR)^2]$ and $G_R(r) \propto \exp(-|r|/R)$, by Fourier duality. The limits $R \ll L$ and $R \gg L$ lead respectively back to the white noise and Brownian motion cases in Figs. B1 and B2.

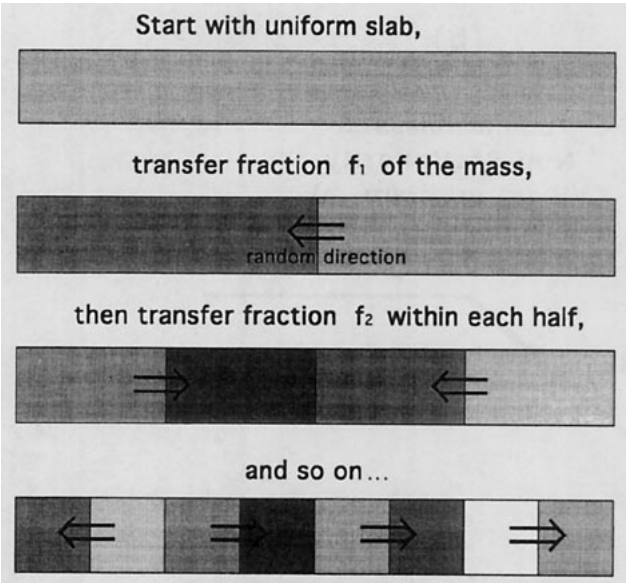

FIG. B4. Construction of a mass-conserving multiplicative cascade model. Starting with a homogeneous slab of material, one first transfers a fraction f_1 of the mass from one half to the other in a randomly chosen direction. This is equivalent to multiplying the originally uniform density field on either side by a factor of $1 \pm f_1$. The same procedure is repeated recursively at smaller scales using fractions f_i ($i = 2, 3, \cdots$) on segments of size $r_{i-1} = 1/2^{i-1}$. If, independent of i, we take $f_i = 1 - 2p$ ($0 < p < 1/2$), we have a singular model originally proposed by Meneveau and Sreenivasan (1987b) for the highly intermittent yet stationary dissipation field in turbulence. If $p \to 0$ and constant fields if $p \to 1/2$, δ Dirac generalized functions occur. If $f_i = (1 - 2p)r_{i-1}^H$ with $0 < p < 1/2$ and $H > 0$, we obtain Cahalan et al.'s (1994a) bounded cascade models. Marshak et al. (1994) show that these models are patently nonstationary for scales $r \ll r_{1/H} = 2^{-1/H}$, which acts as an integral scale (cf. Fig. B3) and stationary, by construction, at larger scales.

proportional to $|x|$, and the two-point autocorrelation function

$$G(x, r) \propto |x| + |x + r| - |r|, \qquad \text{(B5)}$$

depends explicitly on x as well as r. So Brownian motion is nonstationary, $\langle \varphi(x) \rangle \equiv 0$ notwithstanding; at the same time, it is stochastically continuous since $\langle [\varphi(x + r) - \varphi(x)]^2 \rangle \propto r$, independently of x. Now compare the two zero-crossing sets: for white noise, it is space filling (dimension 1); here, it is sparse (fractal dimension 1/2). This is typical of nonstationary behavior, most probable values are rarely revisited within finite time, a characteristic that often leads the unwary to see trends and oscillations where there are none.

3) Ornstein–Uhlenbeck processes are our third and last example. They also have Gaussian pdf's and a nonscaling autocorrelation function

$$G_R(r) \propto \exp(-|r|/R), \qquad \text{(B6)}$$

where $R > 0$ is the integral scale mentioned in sections 6 and 7. They are stochastically continuous since Eqs. (B3) and (B6) lead to $\langle [\varphi_R(x + r) - \varphi_R(x)]^2 \rangle = 2G_R(0)[1 - \exp(-|r|/R)]$, which goes to zero as $|r|$. Figure B3 shows a realization of $\varphi_R(x)$ with length $L = 8R$.

Ornstein–Uhlenbeck processes are solutions of the stochastic ODE

$$\frac{d}{dx}\varphi_R + \frac{1}{R}\varphi_R(x) = \text{white_noise}(x), \qquad \text{(B7)}$$

with a random initial condition (e.g., Arnold 1974). We have $\varphi_R(\cdot) \to$ Brownian motion as parameter $R \to \infty$ and white noise as $R \to 0$. In essence, Fig. B3 shows eight statistically similar but independent portions of Brownian motion put end to end. If we extract one point from each of these portions (e.g., the large dots in Fig. B3), we would again have white noise. Thus, we have a process that is nonstationary at small scales but stationary at large ones.

b. Spectral criterion for stationarity in scale-invariant datasets: $\beta < 1$

For a stationary scale-invariant process, we have a power law in $|r|$ for the autocorrelation function in Eq. (B1):

$$G(r) \propto |r|^{-\mu}, \quad \mu > 0. \qquad \text{(B8)}$$

The exponent μ must be positive, since we expect less correlation as $|r|$ increases. The singularity at $r = 0$ automatically implies stochastic discontinuity. The Wiener–Khinchine theorem states that, under stationary conditions, $G(r)$ and $E(k)$ form a Fourier transform pair. (However, unlike autocorrelation analysis, spectral analysis is not restricted to stationary cases, since a translation in x leads to a phase shift in $\tilde{\varphi}(k)$ that leaves $E(k)$ unchanged.) Fourier transform tables (e.g., Gradshteyn and Ryzhik 1980) tell us that the duality between Eqs. (2) and (B8) requires

$$0 < \beta = 1 - \mu < 1 \qquad \text{(B9)}$$

for the exponents. This gives us a simple spectral criterion for stationarity ($\beta < 1$) discussed by, among others, Mandelbrot (1977).

It is important to note that the exponent relationship Eq. (B9) applies only when $\varphi(x)$ has both power-law properties Eqs. (2) and (B8); otherwise, it is meaningless. The white noise limit $\beta \to 0$ yields $G(r) \propto \delta(r)$, not $\mu = 1$. On the other hand, the $1/f$ noise limit $\beta \to 1$ does not lead to $\mu = 0$, that is, to $G(r) =$ constant (all points equally correlated); $\beta = 1$ is borderline between stationarity and nonstationarity, and $\mu \to 0$ just means that we anticipate very long range correlations, not only longer than any exponential law as in Eq. (B5) but longer than any power law in Eq. (B8) that is still integrable at $r = 0$ (Davis et al. 1994b).

In summary, datasets with $\beta < 1$ are more likely to yield meaningful results for $G(r)$ in Eq. (B1), at least in the range of scales where Eq. (2) applies.

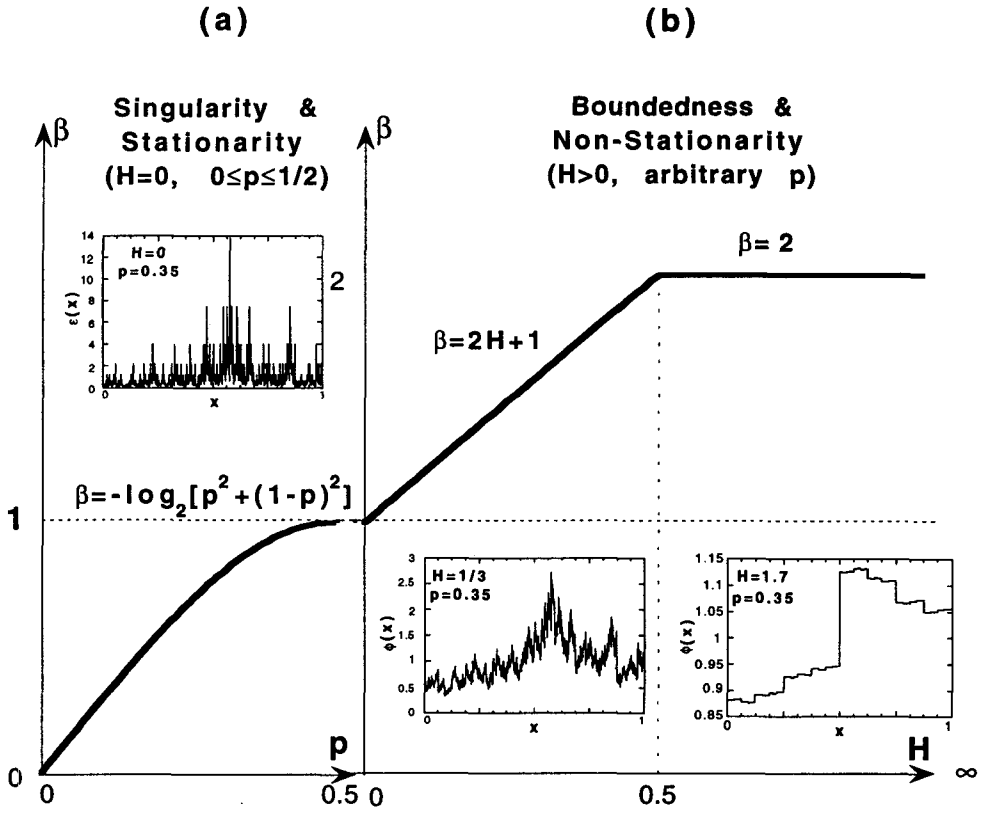

FIG. B5. Spectral exponents and examples of the multiplicative cascade model in Fig. B4. (a) In the stationary/singular case $H = 0$, β is determined by p, going from the δ-function case at $p = 0$ with $\beta = 0$ to the weakly variable limit $p \to 1/2^-$, where $\beta \to 1^-$. For the (leftmost) inset we have taken $p = 0.35$, the value that best reproduces the statistical properties of Meneveau and Sreenivasan's (1987a) turbulence data. All these $H = 0$ cases with $\beta \leq 1$ are almost everywhere discontinuous since $\mu > 0$ in Eqs. (B8) and (B9). (b) In the nonstationary/bounded case $H > 0$, β is given in the small-scale limit by $\min[2H, 1] + 1$ (independently of p), going from the $1/f$ noise limit ($H \to 0^+$) with $\beta \to 1^+$ to the extreme ($H \to \infty$) case of a Heaviside step at $x = 0.5$, where $\beta = 2$, due to the single discontinuity. For the (middle and rightmost) insets, we have taken $H = 1/3$, the best fit for Cahalan and Snider's (1989) LWP data, and $H = 1.7$. All cases with $H \geq 1/2$ have a finite number of jumps, leading invariably to $\beta = 2$.

Conversely, we are likely to find either small values of μ in a fit of $G(r)$ to Eq. (B8) in log–log axis or R not small with respect to the outer scale L when fitting $G(r)$ to Eq. (B6) in semilog axes for datasets with $\beta > 1$. Both results are spurious in the sense of dependence on the realization and the amount of data in each one. In the absence of spectral information, these findings should be viewed as symptoms of nonstationarity in the data for the corresponding range of scales.

c. *Related stationary and nonstationary models and atmospheric fields*

We illustrate the (non)stationarity criterion $\beta\,(>)< 1$ with synthetic and physical examples:

- Integration ($\beta \to \beta + 2$) can be used to transform stationary processes ($|\beta| < 1$) into nonstationary ones ($\beta > 1$) with stationary increments ($\beta < 3$), for example, white noise ($\beta = 0$) leads to Brownian motion ($\beta = 2$).
- Conversely, gradients (nearest-neighbor differences) of nonstationary processes are generally stationary. As an example, we recall that turbulent *velocity* signals are nonstationary in the inertial subrange ($\beta \approx 5/3$), whereas the squared velocity gradients are representative of the stationary but highly intermittent *dissipation* field (Meneveau and Sreenivasan 1987a) and are currently modeled with singular multiplicative cascades such as Meneveau and Sreenivasan's (1987b) "p model" in Figs. B4 and B5a. These models are stationary by construction, and we have $\mu = \log_2[1 + (1 - 2p)^2] > 0$, $0 < p < 1/2$, in Eq. (B8), hence, $\beta < 1$ from Eq. (B9).
- In section 7, we show that we can treat the liquid water content data from FIRE 87 in Figs. 3a–e and 9a like turbulent velocity in this respect: these time series

are nonstationary, whereas their absolute gradients (cf. Fig. 9b) are stationary, suggesting that a singular cascade can be used to model the latter field. A p model with $p \approx 0.25$ would fit our ensemble-average spectrum with $\beta \approx 0.7$ in Fig. 10.

• Cahalan and Snider (1989) investigate liquid water path (vertically integrated LWC) retrieved from microwave measurements of marine Sc during FIRE 87 and observe nonstationary ($\beta \approx 5/3$) behavior. Cahalan et al. (1994a) proposed a simple generalization of the p model illustrated in Figs. B4 and B5b. The new parameter $H > 0$ is used to "tame" the singularities that develop as the p-model cascade proceeds to smaller scales. It is shown to be bounded and nonstationary rather than stationary: $\beta = \min\{2H, 1\} + 1 > 1$ (Marshak et al. 1994).

We must bear in mind that datasets can be at once stationary at some scales (typically, the larger ones) and nonstationary at others (typically, the smaller ones). This however requires a statistically "robust" scale break, that is, not traceable to a fluke observed in a single realization. For instance, in very long wind tunnel turbulent velocity signals, one finds qualitatively different behavior for scales larger and smaller than the outer scale of the system (in this case, the tunnel diameter): at large scales, decorrelation is achieved and stationarity prevails, whereas at small scales long-range correlations and nonstationarity prevail, maintained by inertial-range dynamical processes. We observe evidence for a similar transition in our LWC data (cf. Fig. 7b).

REFERENCES

Albrecht, B. A., D. A. Randall, and S. Nicholls, 1988: Observations of marine stratocumulus clouds during FIRE. *Bull. Amer. Meteor. Soc.*, **69**, 618–626.

Arnold, L., 1974: *Stochastic Differential Equations, Theory and Applications.* Wiley and Sons, 228 pp.

Austin, P., Y. Wang, R. Pincus, and V. Kujala, 1995: Precipitation in stratocumulus clouds: Observational and modeling results. *J. Atmos. Sci.*, **52**, 2329–2352.

Baker, B., 1992: Turbulent entrainment and mixing in clouds: A new observational approach. *J. Atmos. Sci.*, **49**, 387–404.

Brenguier, J. L., 1992: Statistical properties of the droplet spatial distribution in stratocumulus. *Proc. of 11th Int. Conf. on Clouds and Precipitation,* Vol. 1, Montreal, PQ, Canada, International Commission on Clouds and Precipitation and International Association of Meteorology and Atmospheric Physics, 125–128.

Cahalan, R. F., and J. H. Joseph, 1989: Fractal statistics of cloud fields. *Mon. Wea. Rev.*, **117**, 261–272.

——, and J. B. Snider, 1989: Marine stratocumulus structure. *Remote Sens. Environ.*, **28**, 95–107.

——, W. Ridgway, W. J. Wiscombe, T. L. Bell, and J. B. Snider, 1994a: The albedo of fractal stratocumulus clouds. *J. Atmos. Sci.*, **51**, 2434–2455.

——, ——, ——, S. Gollmer, and Harshvardhan, 1994b: Independent pixel and Monte Carlo estimates of stratocumulus albedo. *J. Atmos. Sci.*, **51**, 3776–3790.

Cess, R. D., and Coauthors, 1989: Interpretation of cloud–climate feedback as produced by 14 atmospheric general circulation models. *Science*, **245**, 513–516.

Corrsin, S., 1951: On the spectrum of isotropic temperature fluctuations in isotropic turbulence. *J. Appl. Phys.*, **22**, 469–473.

Davis, A., 1992: Radiation transport in scale-invariant optical media. Ph.D. thesis, McGill University, 247 pp.

——, A. Marshak, W. Wiscombe, and R. Cahalan, 1994a: Multifractal characterizations of non-stationarity and intermittency in geophysical fields, observed, retrieved, or simulated. *J. Geophys. Res.*, **99**, 8055–8072.

——, ——, and ——, 1994b: Wavelet-based multifractal analysis of nonstationary and/or intermittent geophysical signals. *Wavelets in Geophysics,* E. Foufoula-Georgiou and P. Kumar, Eds., Academic Press, 249–298.

Duroure, C., and B. Guillemet, 1990: Analyse des hetérogeneités spatiales des stratocumulus et cumulus. *Atmos. Res.*, **25**, 331–350.

Falconer, K. J., 1990: *Fractal Geometry Mathematical Foundations and Applications.* J. Wiley and Sons, 288 pp.

Gerber, H., B. G. Arends, and A. S. Ackerman, 1994: New microphysics sensor for aircraft use. *Atmos. Res.*, **31**, 235–252.

Gradshteyn, I. S., and I. M. Ryzhik, 1980: *Table of Integrals, Series, and Products.* Academic Press, 1160 pp.

King, W. D., D. A. Parkin, and R. J. Handsworth, 1978: A hot-wire liquid water device having fully calculable response characteristics. *J. Appl. Meteor.*, **17**, 1809–1813.

——, C. T. Maher, and G. A. Hepburn, 1981: Further performance tests on the CSIRO liquid water probe. *J. Appl. Meteor.*, **20**, 195–202.

Kloesel, K. A., B. A. Albrecht, and D. P. Wylie, 1988: FIRE marine stratocumulus observations—summary of operations and synoptic conditions. FIRE Tech. Rep. 1, Dept. of Meteorology, The Pennsylvania State University, University Park, PA, 171 pp.

Kolmogorov, A. N., 1941: Local structure of turbulence in an incompressible liquid for very large Reynolds numbers. *Dokl. Akad. Nauk SSSR*, **30**, 299–303.

Kraichnan, R. H., 1967: Inertial ranges in two-dimensional turbulence. *Phys. Fluids*, **10**, 1417–1423.

Lovejoy, S., 1982: Area–perimeter relation for rain and cloud areas. *Science*, **216**, 185–187.

——, and B. Mandelbrot, 1985: Fractal properties of rain and a fractal model. *Tellus*, **37A**, 209–232.

——, D. Schertzer, P. Silas, Y. Tessier, and D. Lavallée, 1993: The unified scaling model of atmospheric dynamics and systematic analysis of scale invariance in cloud radiances. *Ann. Geophys.*, **11**, 119–127.

Malinowski, S. P., and I. Zawadzki, 1993: On the surface of clouds. *J. Atmos. Sci.*, **50**, 5–13.

——, D. G. Baumgardner, and M. Y. Leclerc, 1992: Fractal analysis of high resolution FSSP data. *Proc. 11th Int. Conf. on Clouds and Precipitation,* Vol. 1, Montreal, PQ, Canada, International Commission on Clouds and Precipitation and International Association of Meteorology and Atmospheric Physics, 188–191.

Mandelbrot, B. B., 1977: *Fractals: Form, Chance, and Dimension.* W. H. Freeman, 365 pp.

Marshak, A., A. Davis, R. Cahalan, and W. Wiscombe, 1994: Bounded cascade models as nonstationary multifractals. *Phys. Rev. E*, **49**, 55–69.

Meneveau, C., and K. R. Sreenivasan, 1987a: The multifractal spectrum of the dissipation field in turbulent flows. *Nucl. Phys. B*, **2**, 49–76.

——, and ——, 1987b: Simple multifractal cascade model for fully developed turbulence. *Phys. Rev. Lett.*, **59**, 1424–1427.

Monin, A. S., and A. M. Yaglom, 1975: *Statistical Fluid Mechanics.* Vol. 2. The MIT Press, 683 pp.

Obukhov, A., 1949: Structure of the temperature field in turbulence. *Izv. Akad. Nauk. SSSR. Ser. Geogr.*, **13,** 55–69.

Papoulis, A., 1965: *Probability, Random Variables, and Stochastic Processes.* McGraw-Hill, 583 pp.

Peitgen, H. O., and D. Saupe, 1988: *The Science of Fractal Images.* Springer-Verlag, 312 pp.

Press, W. H., S. A. Teukolsky, W. T. Vetterling, and B. P. Flannery, 1993: *Numerical Recipes in FORTRAN.* 2d ed. Cambridge University Press, 702 pp.

Ramanathan, V., R. D. Cess, E. F. Harrison, P. Minnis, B. R. Barkstrom, E. Ahmad, and D. Hartmann, 1989: Cloud-radiative forcing and climate: Results from Earth Radiation Budget Experiment. *Science,* **243,** 57–63.

Rodi, A. R., J. L. Brenguier, and J. P. Chalon, 1992: Case study of cumulus microstructure with the new FFSSP. *Proc. 11th Int. Conf. on Clouds and Precipitation,* Vol. 1, Montreal, PQ, Canada, International Commission on Clouds and Precipitation and International Association of Meteorology and Atmospheric Physics, 169–172.

Rys, F. S., and A. Waldvogel, 1986: Analysis of the fractal shape of severe convective clouds. *Fractals in Physics,* L. Pietronero and E. Tosatti, Eds., Elsevier, 461–464.

Sèze, G., and L. Smith, 1990: On the dimension of cloud boundaries. *Proc. Seventh Conf. on Atmospheric Radiation,* San Francisco, CA, Amer. Meteor. Soc., 47–57.

Sui, C.-H., and K. M. Lau, 1992: Multiscale phenomena in the tropical atmosphere over the western Pacific. *Mon. Wea. Rev.,* **120,** 407–430.

Weng, H., and K.-M. Lau, 1994: Wavelets, period doubling, and time–frequency localization with application to organization of convection over the tropical western Pacific. *J. Atmos. Sci.,* **51,** 2523–2541.

Yano, J. I., and Y. Takeuchi, 1987: The self-similarity of horizontal cloud pattern in the intertropical convergence zone. *J. Meteor. Soc. Japan,* **65,** 661–667.